ELM resolved energy distribution studies in the JET MKII Gas Box divertor using infra-red thermography

T.Eich‡, P.Andrew[1], A.Herrmann, W.Fundamenski[1], A.Loarte[2], R.A.Pitts[3] and JET-EFDA contributors†

Institut für Plasmaphysik, Association EURATOM-IPP, Boltzmannstrasse 2, 85748 Garching, Germany

[1] EURATOM-UKAEA Fusion Association, Culham Science Centre, Abingdon, Oxfordshire, OX14 3EA, UK

[2] CSU-EFDA, Institut für Plasmaphysik, Association EURATOM-IPP, Boltzmannstre 2, 85748 Garching, Germany

[3] Association EURATOM, CRPP-EPFL, 1015 Lausanne, Switzerland

This work has been conducted under the European Fusion Development Agreement.

Abstract. Using infra-red (IR) thermography, power loads onto the MKII Gas-Box divertor targets have been investigated in Type-I ELMy H-Mode plasmas at JET in medium current discharges (I_p =2.6MA and B_T =2.7T). Heat fluxes are calculated from the measured divertor target tile surface temperatures taking into account the influence of co-deposited surface layers on tile surfaces. This is particularly important when estimating the energy deposition during transient events such as ELMs. Detailed energy balance analysis is used, both from IR and tile embedded thermocouples, to demonstrate an approximately constant ELM-averaged in/out divertor target asymmetry of ≈ 0.55 and to show that the ELM in/out energy deposition ratio ranges from 1:1 to 2:1. The inter-ELM in/out ratio is close to the ELM averaged value at low pedestal collisionalities and decreases down to values close to zero when the inner target plasma detaches at the highest pedestal collisionalities. The fraction of ELM transported energy is observed to behave differently for the inner and outer divertor. At higher pedestal collisionalities nearly the full inner target load is due to the ELMs whereas for the outer target the ELM transported energy never exceeds values of $\approx$ 0.3 of the total energy deposited there. The fraction of ELM energy arriving at the divertor compared to the pedestal loss energy in JET is found to be in the range of 0.75 for small ELMs down to 0.4 for large ELMs systematically decreasing with normalized ELM size. Since ITER is bound to use small ELMs the corresponding ELM wall load therefore is expected to be small. The latter experimental result is in fair agreement to the observation that larger ELMs tend to travel faster across the SOL than smaller ELMs. However, a comparison of the presented data to models of ELM perpendicular transport is not conclusive due to the large experimental errorbars and uncertainties in the model assumptions.

‡ E-Mail corresponding author: thomas.eich@ipp.mpg.de

† Annex 1 of Pamela J et al. Overview of JET Results, Nuclear Fusion **45**, p.S63-S85 (2005)

1. Introduction

Key issues which remain unresolved for a next step fusion device such as ITER [1] are the handling of the steady-state power exhaust of a burning fusion plasma and the heat load due to fast transient events [2] like disruptions [3] or edge localised modes (ELMs)[4]. For ITER, the Type-I ELMy H-Mode [5] is currently envisaged as the $Q_{DT} = 10$ burning plasma standard scenario and is the focus of studies reported here.

A dedicated set of discharges has been performed during the JET MKII Gas Box divertor campaign to estimate the divertor target power deposition characteristics both during and in-between Type-I ELMs by means of infra-red (IR) thermography measurements. IR measurements were already executed for the previous JET divertor campaigns MKI[6] and MKII [7] and compared to the results found here. Neutral Beam Injection (NBI) heating power, P_{NBI} , density, n_{av} , triangularity, δ_{95} and safety factor, q_{95} scans have been executed during these experiments. In each case, the plasma magnetic configuration and NBI timing have been adjusted to obtain the best possible infra-red (IR) measurements in terms of data acquisition speed and duration, spatial resolution and the estimation of the surface temperature from measured photon fluxes.

The paper is organised as follows: Section 2 introduces some details of the discharges performed in the course of this experiment and describes the IR diagnostic along with examples of the temperature profiles on the divertor target areas. Some effort is also devoted to a description of the method used to derive the heat flux, including uncertainties due to surface layer effects on the estimation of deposited power and energy. Section 3 presents the time evolution of the divertor target temperature, power and energy, discriminating the ELM and the inter-ELM periods and compares the IR based estimations of energy on the inner and outer targets with thermocouple measurements. To illustrate the important physics output provided by the diagnostic and the associated data processing, results will be presented showing the link between energy deposited in the SOL by the ELM and that retrieved at the divertor targets.

2. Experiment

2.1. Experimental data base of IR-optimised discharges

Table 1 summarises all JET discharges analysed in this paper and represents the small fraction of JET Gas-Box divertor Type-I ELMy H-Modes in which the magnetic configuration (see Figure 1) has been adapted to optimise the IR view on the divertor strike points. The abbrevations used in Table 1 mean (#) shotnumber, (Δt) time interval of flat top phase within discharge used for data analysis, (n_{av}) line averaged density for entire plasma volume, (I_p) plasma current, (B_T) toroidal magnetic field, (δ_{95}) triangularity of magnetic field configuration at poloidal magnetic flux surface of 95% of total poloidal magnetic flux, (q_{95}) safety factor at same flux surface, (P_{NBI}) neutral beam heating power, (f_{ELM}) ELM frequency, (E_{plasma}) plasma stored energy, (Gas) gas puffing rate by inner divertor gas valve, (P_{IR}/P_{NBI}) fraction between radiated power

Table 1. Overview of the main plasma parameters for the JET Type-I ELMy H-Mode discharges analysed in this paper. Each employs a magnetic equilibrium optimised for IR divertor target power deposition measurements (see Figure 1). For the meaning of the abbrevations see text.

#	Δt	n_{av}	I_p	B_T	δ_{95}	P_{NBI}	q_{95}	f_{ELM}	E_{plasma}	Gas	$\frac{P_{IR}}{P_{NBI}}$	ν^*_{ped}
-	s	$\frac{10^{19}}{m^3}$	MA	T	1	MW	1	Hz	MJ	$\frac{10^{22}}{s}$	%	1
53764	23-24	3.7	1.5	2.6	0.22	9.5	5.0	11	3.1	0.0	49.5	0.04
53765	18-19	5.5	2.5	2.6	0.21	13.7	2.8	17	5.6	0.0	75.2	0.16
53765	23-24	5.5	2.5	2.6	0.21	17.3	2.8	15	6.1	0.0	56.7	0.17
53767	18-19	5.8	2.5	2.6	0.20	16.2	2.9	18	6.0	0.0	67.3	0.21
53767	23-24	7.7	2.5	2.6	0.20	16.2	2.9	34	5.3	2.4	50.6	0.40
53768	18-19	5.9	2.5	2.6	0.31	16.2	2.8	29	5.5	0.0	63.5	0.34
53768	23-24	7.5	2.5	2.6	0.31	13.7	2.8	38	4.6	4.0	43.8	0.37
53770	18-19	6.7	2.5	2.6	0.30	14.0	3.3	12	5.9	0.0	76.4	0.28
53770	23-24	7.9	2.5	2.6	0.30	13.0	3.3	23	5.4	1.7	51.5	0.43

and neutral beam heating power, (ν^*_{ped}) collisionality at pedestal top, for a definition of ν^*_{ped} see section 3.3.

All the discharges in Table 1 were executed on a single operation day, minimising the influences of possibly time varying parameters that can arise from wall conditioning or changes in the divertor target surface. Such effects have been reported in a variety of experiments and notably on the ASDEX Upgrade [8, 9], TEXT-Upgrade [10] and JET itself [7, 11, 12]. Detailed studies of the influence of surface properties on the estimation of the divertor target surface temperatures and possible deviations from ideal Planck radiators may be found in Refs. [13, 14, 15, 16].

Thanks both to the relatively long flat top phase of JET discharges compared to the energy confinement time and the availability of NBI powers of up to 16 MW for 10 seconds, a two-point scan of any given parameter was often possible in a single discharge. As a result, 9 different plasma conditions were obtained using just 5 discharges. An example is shown in Figure 2, illustrating two phases of one such pulse. For a detailed study of the ELM power load, fast magnetic signals with sampling rates of 100kHz are used to derive the sudden drop of plasma stored energy due to the ELM event. Acquisition of these fast signals is usually restricted to an 800ms window at the end of the second phase in each discharge as indicated in Figure 2. This results in larger errorbars for the ELM energy loss during the first phase, since only a reduced sampling rate of 30 Hz is available for data analysis in this period.

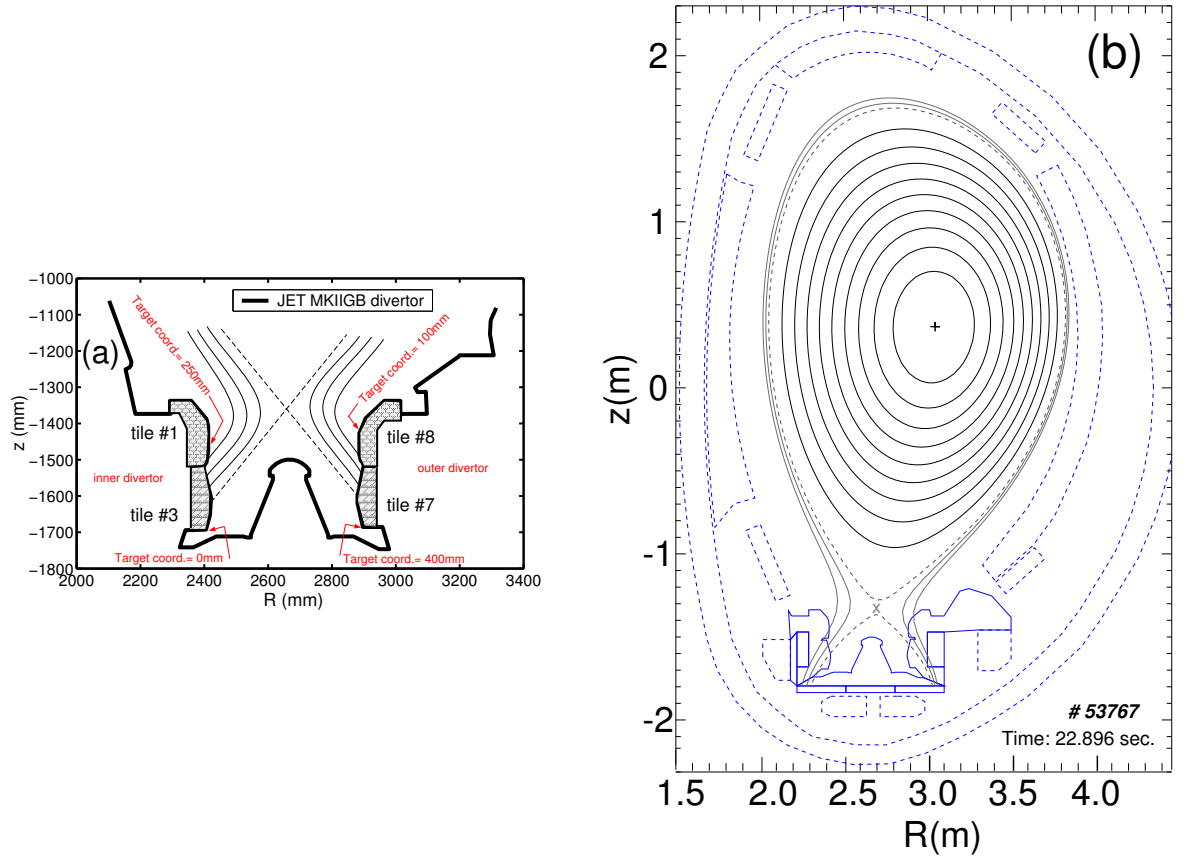

Figure 1. (a) Geometry of the MKII Gas-Box divertor at JET including the magnetic field structure derived with EFIT equilibrium reconstruction in the divertor region and (b) for the full poloidal cross section. All discharges have been performed with strike point positions optimised for IR measurements.

2.2. Basic properties of the 2D IR system

The IR camera used in these JET studies employs a Cadmium-Mercury-Telluride (Cd-Hg-Te) array with 128 lines × 128 columns viewing the Gas-Box divertor tangentially. Smaller effective array sizes can be chosen using appropriate software settings. By way of example, Figure 3 shows a frame of the IR surface temperature distribution corresponding to one of the inter-ELM phases in pulse #53767 (see Fig.2). For the work reported here a reduced array size of 62 lines x 128 columns has been used throughout. The camera reads out two lines simultaneously, beginning from the centre of the detector array towards both the top and bottom as shown by the line index on the left and corresponding times on the right of Figure 3.

An optical split in the periscope relay optic system divides the field of view such that both inner and outer divertors can be simultaneously observed. The spatial resolution of the optic system is given by the distortion due to the periscope and the finite pixel sizes introducing an instrument function. This can be described by the convolution of the viewing geometry with a Gaussian of full width at half maximum value of 7.1mm when referred to the outer target coordinates and 5.1mm when referred to the inner

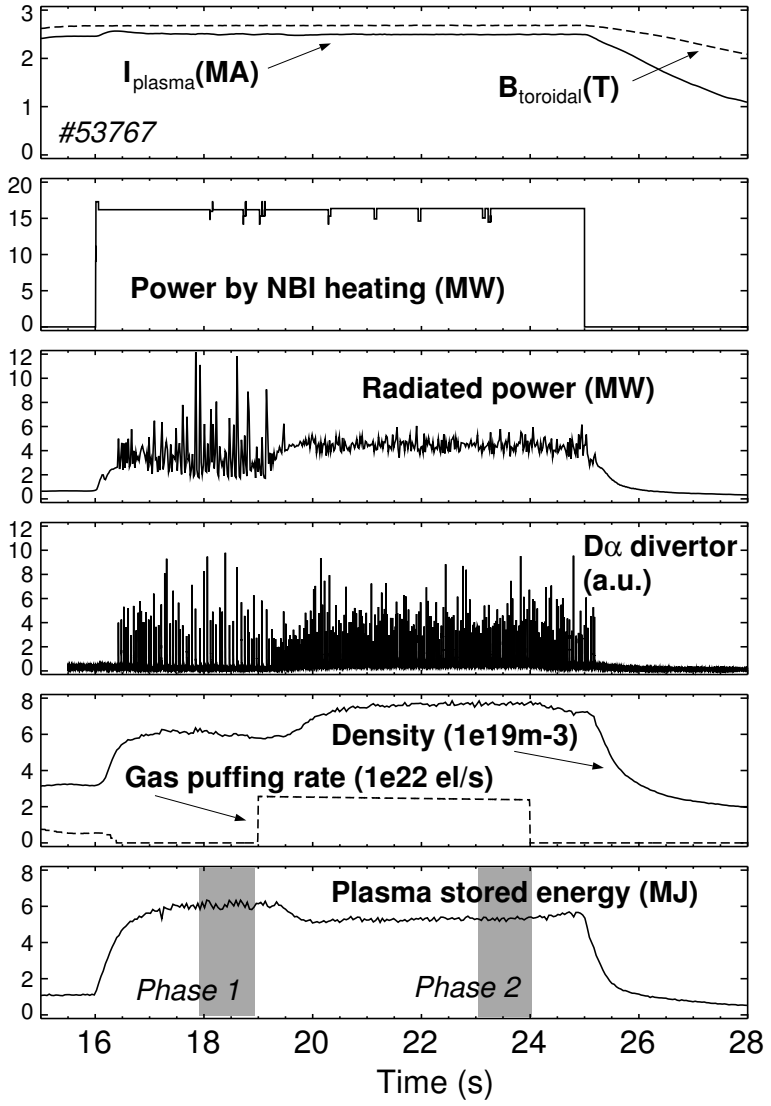

Figure 2. Temporal evolution of the plasma parameters of discharge #53767, a typical example of an IR optimised Type-I ELMing H-Mode. Two different phases can be distinguished: the period without gas fuelling around 19.0 - 20.0 seconds and a later phase during with gas fuelling around 23.0-24.0 seconds with a resulting higher line averaged density.

target (see Table 2).

The custom built detector array is sensitive to photons in the IR wavelength range from 3.0-5.0μm and is extremely flexible regarding acquisition of the 12bit IR signals. The configuration applied for the IR-optimised discharges is summarised in Table 2. The camera must be able to resolve both the inter-ELM power deposition, with typical target temperatures from 80^oC up to 1800^oC and the temperature rise during ELMs, typically several hundred degrees Celsius. To provide a large enough dynamic range, the detector amplification is set and calibrated such that the output signal is roughly proportional to the logarithm of the incoming photon fluxes, with a resulting temperature resolution for single pixels of $\approx 5^oC$ for 200^oC and $\approx 50^oC$ at 1600^oC .

Table 2. Specifications of the 2D IR system at JET as used to obtain the data analysed in this paper.

Sensitivity range	3.0-5.0μm
Detector Full Size	128 lines$\times$ 128 columns
Detector Size used	62 lines x 128 columns
Frame time	2.1 ms
Profile averaging time for inner target	737μs
Profile averaging time for outer target	469μs
Line time	67μs
Integration time	10μs - 60μs
Dynamic range	80-1800^oC
Data recording length	12 seconds
Spatial resolution at strike line: inner poloidal	5.1 mm
Spatial resolution at strike line: inner toroidal	5.5 mm
Spatial resolution at strike line: outer poloidal	7.1 mm
Spatial resolution at strike line: outer toroidal	17 mm

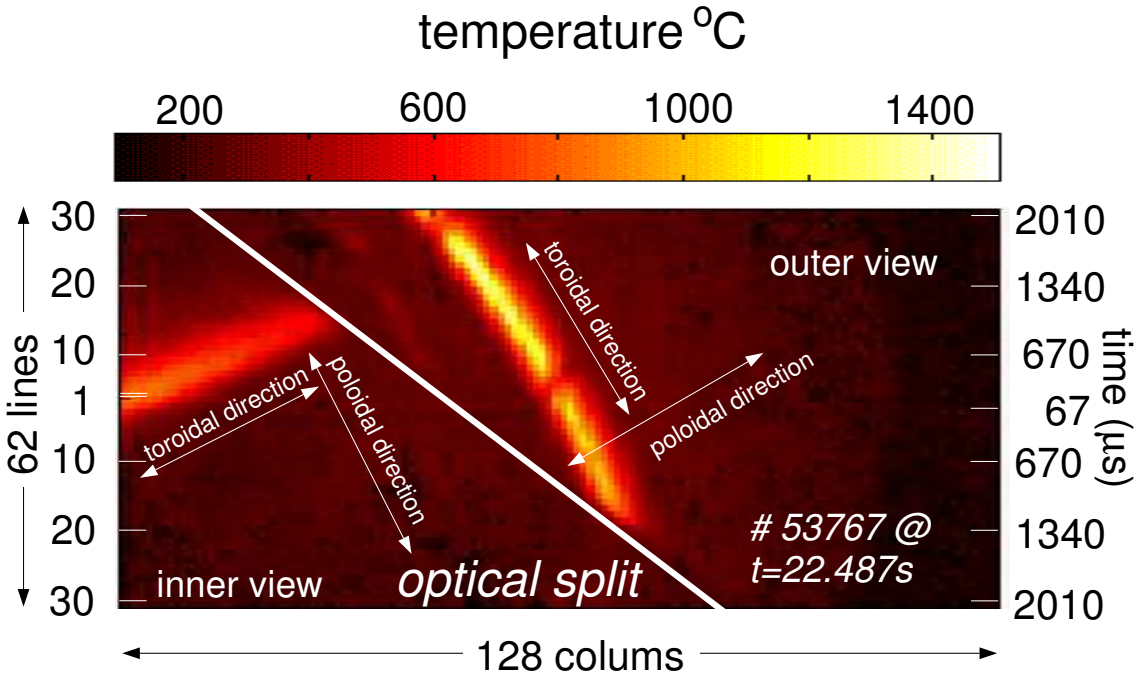

Figure 3. The JET IR detector measures the temperature distribution at both divertor strike zones. Line pairs are read out simultaneously, with each pixel corresponding to a unique point in space and time. An optical split subdivides the detector array into an outer and an inner divertor view. The strike lines of the inner and outer divertor legs are clearly visible (see Figure 4 for an illustration of how this distribution maps to the real target geometry).

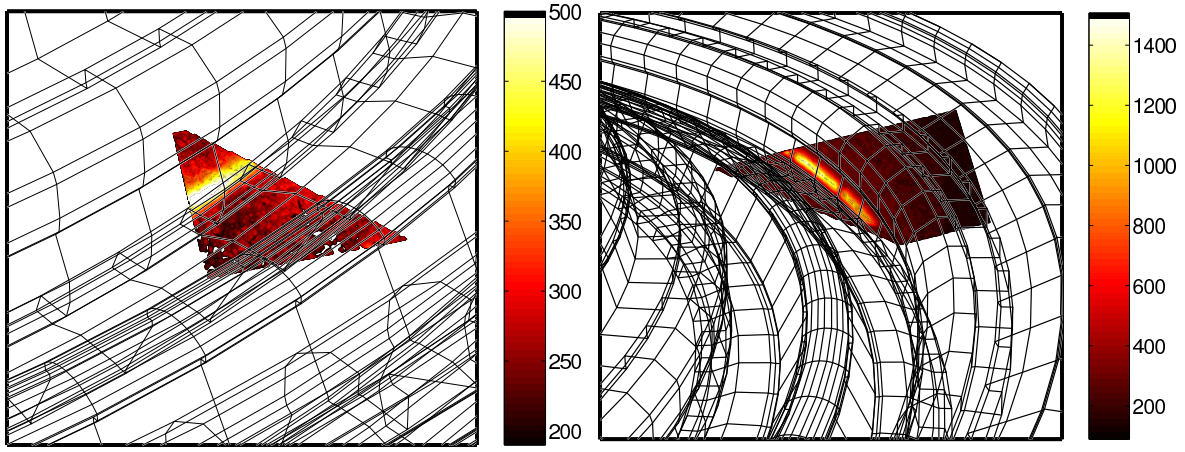

Figure 4. Optically split tangential IR view mapped onto the (a) inner and (b) outer target geometries, illustrating how the IR optimised magnetic configuration places strike points yielding the best spatial resolution and is remote from tile edges. The temperature (in ^oC) data are identical to that shown in Figure 3.

A pre-defined pixel set observing the same poloidal, but varying toroidal positions is routinely averaged to obtain a single poloidal profile measurement. In this way, the pixel noise is reduced but possible variations of the temperature profile along the toroidal direction are neglected. The temporal resolution of the IR system is determined by two different timescales:

- The read-out time of every line of pixels (line time) during which only restricted spatial temperature profile information can be obtained from different toroidal and poloidal locations. In this case, assuming toroidal symmetry of the ELM power deposition, coherent ELM-averaging can be used to reconstruct the power profile evolution with time resolution equal or better than the line time when referred to an external, faster signal. Further details regarding this procedure are beyond the scope of the present contribution but can be found in Ref [17].
- The frame time is the time over which the complete detector array is read out (62 lines x 128 columns for the experiments reported here). For every frame a single poloidal profile is computed, reducing scatter in the temperature estimation by averaging many pixels. The frame time is the basic timescale in this work and is fixed for all analysed cases to 67μs /line x 62 lines x 1/2 = 2.1ms. The factor 1/2 is a consequence of two lines being read out simultaneously by the detector electronics. A subset of 11 and 7 lines are used to reconstruct the poloidal profiles on the inner and outer target, respectively, yielding averaging times of 67μs /line x 11 lines = 737μs for the inner view and 67μs /line x 7 lines = 469μs for the outer view (see also Table 2).

2.3. In-Situ calibration of the IR system

All components of the IR system at JET have been carefully calibrated using a blackbody source. This is first performed for the detector array alone, and then for the detector plus relay optics, by placing the source inside the JET vacuum vessel roughly 5 weeks after the end of plasma operation plus some months of machine opening. Estimated errors in the IR measurements, associated with the calibration of the IR camera and with toroidal asymmetries have been investigated but found to lead to at most $\approx 5\%$ corrections. One such effect could be due to the formation of e.g. carbon-coatings on the vacuum window through which the divertor is observed, leading to a reduction in the transmission of the shorter IR wavelengths. This would cause a systematic underestimate of the surface temperature for temperatures above 1200^oC , the maximum temperature attainable with the black body source. The observed maximum divertor surface temperature in JET for the discharges analysed in this paper is $\approx 1800^oC$. If this effect were important, strongly heated discharges without gas puffing should then show larger discrepancies in the energy balance. These discharges correspond to the largest energies in Figures 8(a) and (b). As shown in this figure, the differences between IR measurements and those from thermocouple and global power balance are independent of the energy, indicating that this effect is not important in these experiments.

2.4. Transformation of viewing array to measurements of the divertor target profiles

Figure 4 illustrates how the temperature distribution seen by the split optics system is mapped onto the full 3-D target geometry. A transformation code package (*LEOPOLD*) has been written to map these temperature distributions onto target coordinates in terms of the toroidal and poloidal angle. An example of the results of this mapping procedure is shown in Figure 5. While the toroidal angle is given here in degrees, the poloidal angle is drawn for convenience as a target coordinate, describing the increase of the poloidal angle with distance on the target surface from given reference points. In this paper both targets are assigned to their own target coordinates. The inner target coordinate begins from the lower edge in the private flux region and increases vertically upwards towards the scrape-off-layer (SOL) region. The outboard target coordinate begins at the upper edge in the SOL region and increases vertically downwards towards the private flux region. With reference to Figure 1(a), the origin of the target coordinate on the inboard side (tile #3) is located at values of z $\approx$ -1700 mm and at z$\approx$ -1400mm for the outboard target (tile #7).

Sub-areas of the plots in Figure 5 are defined for toroidal averaging so that a poloidal temperature profile with low signal to noise ratio can be determined. The data inside the regions enclosed by the dashed lines are averaged toroidally to obtain profiles over the poloidal target coordinate. The resulting temperature profiles are shown in Figure 6, together with the calculated heat flux profiles for both targets. This method is adequate for events which are slower than the frame time of the camera (2.1ms), but cannot be used for ELMs, where the rise time to maximum heat flux occurs over intervals in the

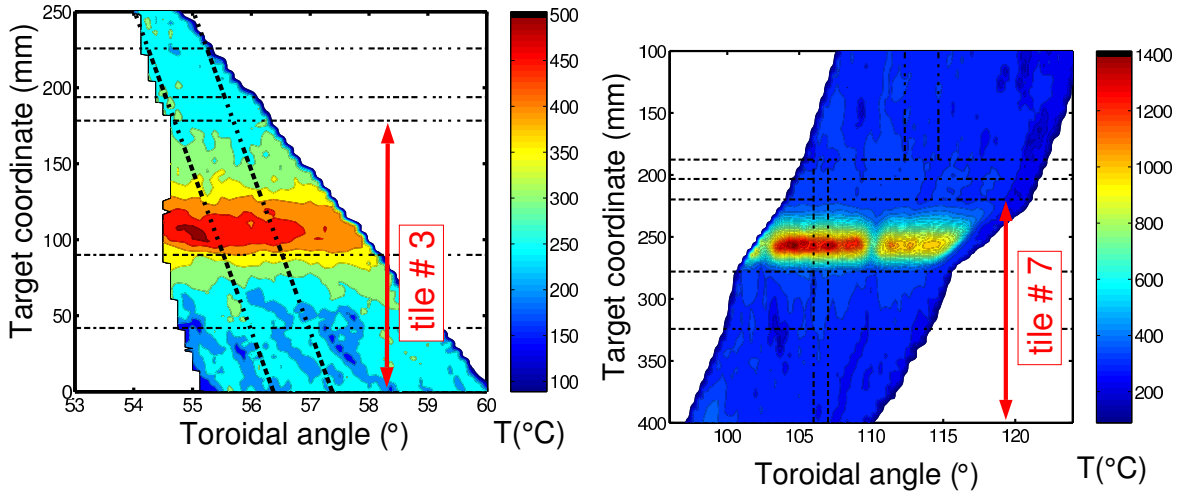

Figure 5. Temperature distributions (in ^oC and derived from Figure 3) for (a) inner and (b) outer target as functions of the toroidal angle and a target coordinate which approximates the poloidal angle. The vertical and inclined dashed lines indicate the sub-areas used for toroidal averaging which are far from the shadowing regions and toroidal tile edges. They are nearly vertical for tile #3 and purely vertical for tile #7. The horizontal dashed-dotted lines indicate the positions of tile edges. Each divertor target surface has a slightly different inclination with respect to the attack angle of the magnetic field line. The strike lines are positioned to provide best possible spatial resolution in the IR field of view.

range of 0.1-0.5ms in JET[17]. Each ELM raises the target surface temperature up to a given value, after which the temperature decreases to the lowest value in the inter-ELM cycle on a timescale of tens of ms. This decrease can be measured accurately enough to allow a determination of the integral ELM energy deposited on the targets.

2.5. Heat flux calculations

All heat flux calculations presented here have been obtained using the *THEODOR* code [18]. Beginning with the temporal evolution of the surface temperature distribution along the poloidal target coordinate, the code computes the heat flux distribution using a 2D slab geometry approximation for the target tiles, introducing the real poloidal target width and an averaged target thickness (e.g. 18cm × 4.2 cm for tile #7). The THEODOR code has been benchmarked against a finite element model [19] in which the tile geometry is described exactly. Errors due to the assumption of slab geometry in THEODOR have been found to be negligible in the derivation of the heat fluxes. The latter are derived by numerically solving the bulk target tile temperature time evolution using

$$\rho_{CFC}(T_{bulk}) \cdot C_{CFC}(T_{bulk}) \frac{dT_{bulk}}{dt} = \nabla q_{bulk} \qquad (1)$$

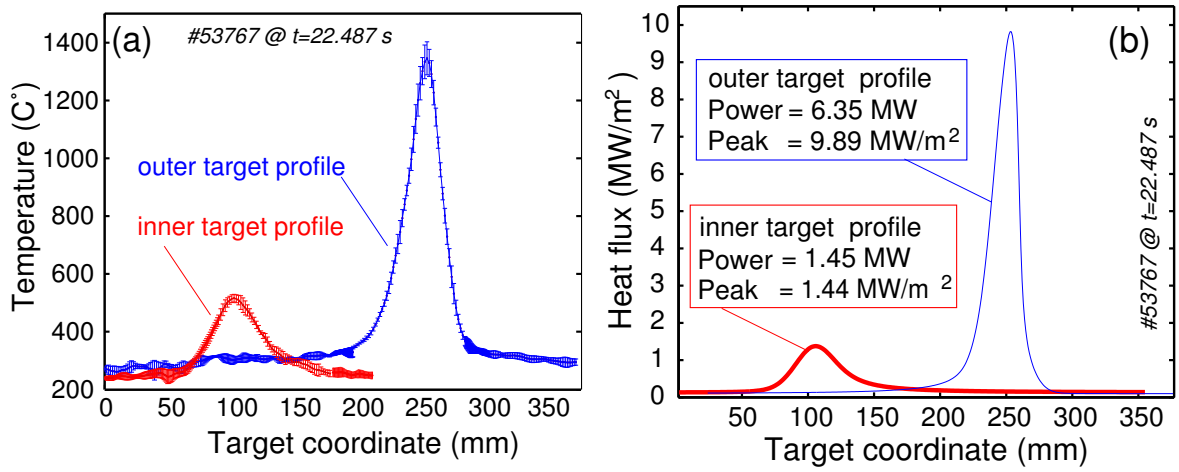

Figure 6. (a) Temperature profiles are computed by toroidally averaging the sub-areas illustrated in Figure 5. The errorbars are estimated only from the standard variation of pixel data in the toroidal direction of the sub-areas. (b) The heat flux profiles are calculated from the temporal evolution of the temperature profiles using the THEODOR code.

Table 3. Material properties for JET Carbon Fibre Composite (CFC) divertor target tiles. The temperature dependent material properties are approximated by a parabolic expression inside the THEODOR code.

T	$\rho_{CFC}(T) \cdot C_{CFC}(T)$	$\kappa_{CFC}^{radial}(T)$	$\kappa_{CFC}^{lateral}(T)$	$\sqrt{\rho_{CFC} C_{CFC} \kappa_{CFC}}$
^oC	$\mathrm{MJ}m^{-3}K^{-1}$	$Wm^{-1}K^{-1}$	$Wm^{-1}K^{-1}$	$Jm^{-2}s^{-1/2}K^{-1}$
0	1.29	318	73.1	20.3
500	2.95	138	31.7	20.2
1000	3.49	122	28.1	20.6

with

$$q_{bulk} = -\kappa_{CFC}(T_{bulk}) \nabla T_{bulk}, \tag{2}$$

where the toroidal direction is ignored and where ρ_{CFC} is the density, C_{CFC} the heat capacity and k_{CFC} the thermal conductivity of the tile material. All three material properties are themselves temperature dependent and are approximated by a parabolic expression inside the code (see Table 3).

2.5.1. Rear and lateral boundary conditions Heat flux boundary conditions are applied on all four sides of the modelled tile geometry. The rear surface is modelled by a heat transmission boundary condition which depends on the difference between the bulk surface temperature and that of the surrounding material. Meanwhile, the lateral sides are assumed to be thermally isolated. At the beginning of a discharge the target is assumed to be at the temperature of the divertor cooling structure,T_{vessel} , maintained constant at around 90^oC by active cooling of the JET divertor structures. Tile embedded thermocouples show that the tile temperature before a given discharge varies from 90^o

to 180^o , generally ratcheting up during the day's operation. In general, the numerical values for the rear and lateral surface boundaries play no significant role for the front side heat flux estimations over the timescale of the diverted phase of the discharge, typically of order 10 seconds.

Values of the (homogeneous) heat flux density for the rear and lateral sides are computed according to

$$q_{rear,lateral} = -0.1 kW m^{-2} K^{-1} \cdot (T_{bulk} - T_{vessel}) \tag{3}$$

approximately describing cooling due both to radiation and to the mechanical fixing of the tiles at the rear sides.

2.5.2. Front surface boundary conditions Plasma material interaction occurs of course primarily on the front surface of the tile, often in such a way that the heat conduction properties of the material are changed. Thin co-deposited surface layers may grow [7, 11, 20, 21], but the quantities required to characterise this layer in terms of its heat conduction behaviour (κ_{layer}) and the layer thickness (d_{layer}) are usually unknown. In addition, the layer morphology differs significantly from that of the bulk material [15]. To avoid the difficult, if not impossible task of attempting to characterise these properties, a heat transmission coefficient α_{sl} [22], is introduced:

$$\alpha_{sl} = \frac{\kappa_{layer}}{d_{layer}}. \tag{4}$$

The temperature, T_{surf} , of the surface layer is thus assumed to be coupled to the bulk temperature, T_{bulk} by a heat flux which is proportional to the difference between both temperatures:

$$q_{layer} = \alpha_{sl} \cdot (T_{surf} - T_{bulk}). \tag{5}$$

Since the surface layer is assumed to have no heat capacity, the incoming heat fluxes from the plasma, the heat flux in the surface layer and the heat flux into the bulk material, are identical:

$$q_{plasma} = q_{layer} = q_{bulk}. \tag{6}$$

Although k_{layer} and d_{layer} cannot be precisely estimated, upper and lower limits for α_{sl} can be determined. These limits define the errorbars on the heat fluxes and will be used throughout this paper. The mean values have been used to derive all heat flux densities and related quantities presented here. In most tokamaks, and JET is no exception, a variety of effects lead to the inner and outer divertor plasmas being quite different (see e.g. [23]). This leads often to different rates of layer growth at the inner and outer targets, especially when carbon is present as in JET. Numerical values of α_{sl} and their respective limits must therefore be derived for each target and for specific machine operating conditions (such as reversed toroidal field operation).

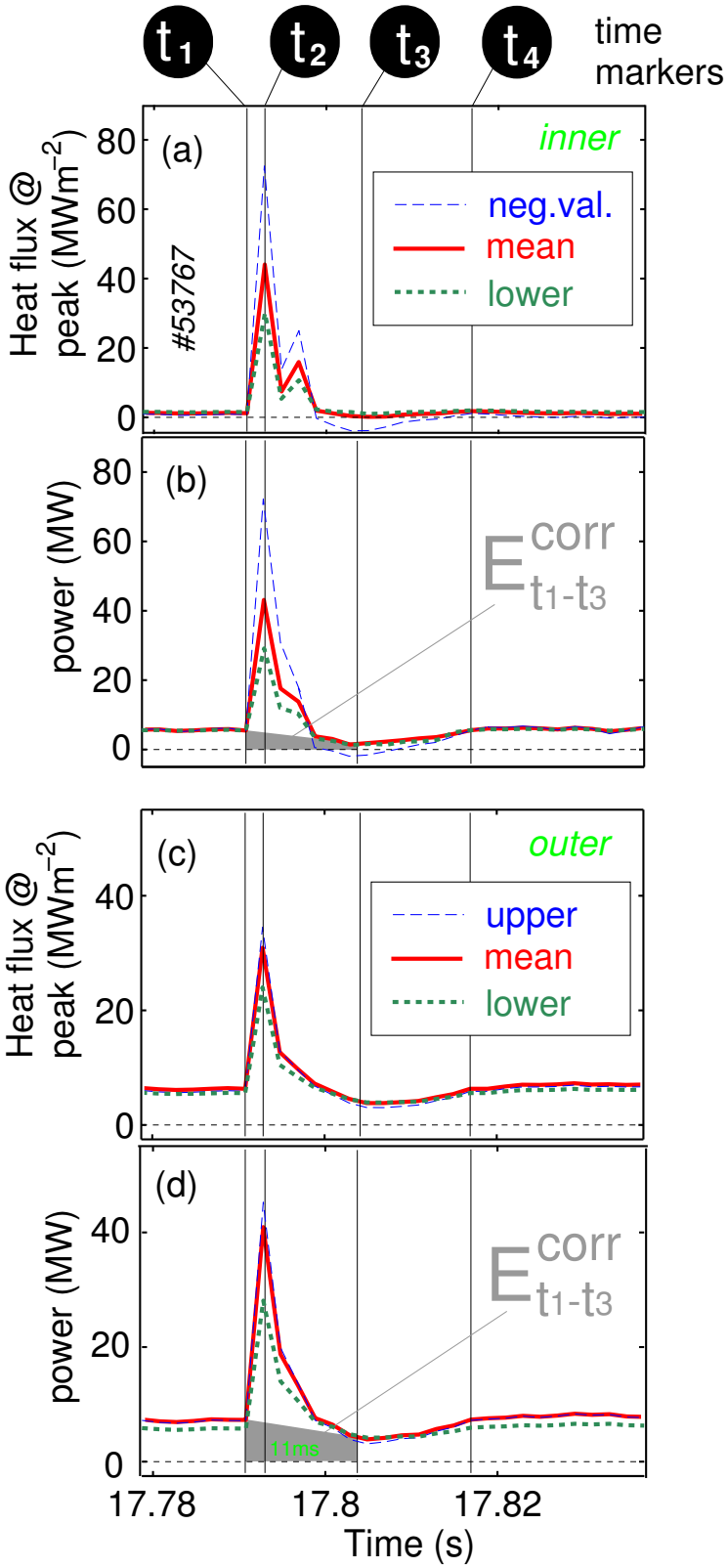

Figure 7. The temporal evolution of the heat flux in the vicinity of the strike points and power calculated with 3 different values of α_{sl}^{inner} and α_{sl}^{outer} (see Table 4). The energy, $E_{t_1-t_3}^{corr}$ represents the uncertainty due to the inter-ELM transport which is taken into account when calculating the ELM deposited energy.

2.6. Estimation of the surface layer coefficient α_{sl} and errorbars for energies

To derive meaningful estimates for α_{sl} during ELMs, different numerical values are used to compute heat fluxes for the measured temperatures. The measured temperature ($T_{IR}(t)$) is derived exclusively from the surface of the bulk material and we denote for convenience $T_{IR}(t) = T_{surf}(t)$. Equation (5) may then be rewritten,

$$T_{bulk}(t) = T_{IR}(t) - \frac{q_{plasma}}{\alpha_{sl}} \tag{7}$$

from which it is clear that T_{bulk} will be strongly influenced by the surface layer when α_{sl} is small. A simple criterion may allow a range of validity for α_{sl} to be defined. This is illustrated for both inner and outer targets in figure 7.

Figure 7 (a)-(d) compiles the heat flux evolution in the strike point vicinity (20mm around the position of the maximum heat flux during the ELM, q_{ELM}^{max}) and the power integrated over the entire target surface (tile #3 and #7, see figure 1). The time markers denote (t_1) as instant before the ELM event, (t_2) at the maximum heat flux, q_{ELM}^{max} , (t_3) at the lowest heat flux in the tail of the ELM, q_{ELM}^{min} and (t_4) after a time interval of 26 ms. The latter corresponds to the time at which the difference in heat fluxes and powers computed using the different α_{sl} are negligible.

Integration of the heat fluxes in the poloidal and toroidal directions yields the deposited powers, P_{IR}^{inner} , P_{IR}^{outer} :

$$P_{IR}^{inner}(t) = 2\pi R_{\#3} \times \int_{0mm}^{210mm} q(s_i, t) ds_i$$
$$P_{IR}^{outer}(t) = 2\pi R_{\#7} \times \int_{100mm}^{345mm} q(s_o, t) ds_o$$

where s_i and s_o are the inner and outer target coordinates (see e.g. Figure 6) and $R_{\#3} = 2.4m$ and $R_{\#7} = 2.8m$ are the major radii of tiles #3 and #7, respectively.

The energy is calculated simply by time integration of the target powers:

$$E(t) = \int_{t_{start}}^{t} P(t') dt'. \tag{8}$$

Toroidal symmetry is assumed for the target heat flux densities at all times during the ELM event. Any deviations from this assumption due to the generic non-toroidal structure of the ELM instability [24] are neglected since it was shown that most of the power arrives as quasi axisymmetric stripes close to the strike line [25].

The energy obtained by integration of the power deposition, taken far from any shadows regions as illustrated in Figure 5, between times (t_1) to (t_4) is denoted as $E_{t_1-t_4}$, such that:

$$E_{t_1-t_4} = \int_{t_1}^{t_4} P(t') dt'. \tag{9}$$

Differences in the derived values of $E_{t_1-t_4}$ for various α_{sl} are due only to the finite integration time, finite temporal resolution and numerical artefacts caused by noise (for the effect of noise on heat flux calculations, e.g. in JET, see [7]). For an ideal

Table 4. Overview of assumed values for α_{sl}^{inner} and α_{sl}^{outer} and resulting maximum (q_{ELM}^{max}) and minimum (q_{ELM}^{min}) peak heat fluxes due to the ELM event in the vicinity of the strike points.

α_{sl}	q_{ELM}^{max}	q_{ELM}^{min}	$E_{t_1-t_4}$	$E_{t_1-t_3}$	$E_{t_1-t_3}^{corr}$	figure	
$\frac{kW}{m^2K}$	$\frac{MW}{m^2}$	$\frac{MW}{m^2}$	kJ	kJ	kJ		
		inner		*target*			
10^7	122	-13.1	170	255	-	not shown	*neg.val.*
100	72.4	-3.8	181	213	-	Fig.7(a)	*neg.val.*
27	40.2	0.0	150	141	12.6	not shown	$\alpha_{sl,upper}^{inner}$
21	33.9	0.4	140	127	18.3	Fig.7(a)	$\alpha_{sl,mean}^{inner}$
17	25.1	1.1	132	115	21.9	Fig.7(a)	$\alpha_{sl,lower}^{inner}$
		outer		*target*			
10^7	38.4	1.8	209	192	-	not shown	-
100	36.3	3.7	201	157	53.3	Fig.7(c)	$\alpha_{sl,upper}^{outer}$
50	35.1	3.8	186	137	58.8	Fig.7(c)	$\alpha_{sl,mean}^{outer}$
33	26.9	4.9	172	120	60.6	Fig.7(c)	$\alpha_{sl,lower}^{outer}$

and infinitely long measurement, any differences between the values of $E_{t_1-t_4}$ calculated using different α_{sl} values would vanish. For an extended discussion about the limits on heat flux estimations in tokamaks see [22].

Table 4 summarises the derived values of α_{sl} and the important quantities used in making the choice of α_{sl} for an example ELM in discharge #53767 at t=17.8 seconds. The parameter q_{ELM}^{max} gives the maximum heat flux density during an (specific) ELM event and q_{ELM}^{min} the minimum value in the tail of the heat pulse. For values of α_{sl}^{inner} above a certain limit, negative heat flux values for q_{ELM}^{min} are observed in the tail of the heat pulse. This is demonstrated for the two highest values for α_{sl}^{inner} in Table 4 by illustrating the temporal evolution of the heat flux and the deposited power in Figure 7, i.e. for the curve denoted as *neg.val.* (negative value). These negative values are known to be artifical [22]. They arise when the temperature of the surface layer falls more rapidly in the tail of the ELM event than the THEODOR code would calculate even with zero heat flux onto the target surface. The only known effect for a real negative heat flux - radiation cooling of the surface - is by several orders of magnitude to small to explain the observed values.

Generally, so called micron-scale hot spots are believed to introduce a further error on the temperature estimation. Since these hot spots have much smaller spatial scales as the typical infra-red spatial resolution, they cause a mixing of regions with different temperatures [16]. For ASDEX Upgrade the resulting errorbar for temperature measurements has been estimated to be in the range of 10% for the temperature range of above 800K which are typically present on the target surfaces in steady state phase in high-powered ELMy H-Modes at JET [16]. More recent studies [26] confirm, that such hot spots will cause negative heat fluxes e.g. in the tail of a transient event such as an ELM. As it is described in detail in [16], the resulting errorbar can be taken into account by introducing (for an assummed clean CFC target tile) a surface layer

coefficient with a numerical value of $\alpha_{sl,error}$=100kW$K^{-1}m^{-2}$. This numerical value provides therefore the smallest uncertainty of heat flux measurements even in absence of any co-deposited surface layer and is consequently used for the upper limit of α_{sl}^{outer}, although even highest values for α_{sl}^{outer}do *not* lead to negative heat fluxes on the outer target as shown in Table 4 and Figure 7.

In contrast for the inner target tile at a certain value of α_{sl}^{inner}, $q_{ELM}^{min} \rightarrow 0$ defining the upper limit for the value of $\alpha_{sl}^{inner}$and reflecting the fact that here co-deposited surface layers are present. Of course, it is not clear (and not expected) that the minimum heat flux after an ELM event should be zero, although it should be much reduced in comparison with the value before the ELM event. This is because the pedestal gradients within the ballooning like inter-ELM transport region are observed to be reduced and the resulting radial transport after the ELM event is transiently lower [27, 28, 29, 30, 31]. Reducing the values for α_{sl}^{inner}still further, q_{ELM}^{min} increases while q_{ELM}^{max} decreases.

In order to derive meaningful errorbars the reciprocal (see equation 7) value of the minimum uncertainty, $1/\alpha_{sl,error}$, is used to introduce the relation between the upper, mean and lower values for α_{sl} given by

$$(\alpha_{sl,upper})^{-1} = \alpha_{sl,mean}^{-1} - \alpha_{sl,error}^{-1} \tag{10}$$

and

$$(\alpha_{sl,lower})^{-1} = \alpha_{sl,mean}^{-1} + \alpha_{sl,error}^{-1} \tag{11}$$

for both divertor targets. These errorbars are regarded to be meaningful since this way $1/\alpha_{sl}^{mean}$ equals the arithmetic mean of $1/\alpha_{sl}^{upper}$ and $1/\alpha_{sl}^{lower}$. This can be easily checked by adding equations 10 and 11 leading to

$$(\alpha_{sl,mean})^{-1} = 1/2 \cdot (\alpha_{sl,lower}^{-1} + \alpha_{sl,upper}^{-1}) \tag{12}$$

. Inserting finally the experimentally motivated values for α_{sl}^{upper} into equations 10 and 11, the values for α_{sl}^{mean} and α_{sl}^{lower} are found to be

$$\alpha_{sl,upper}^{outer} = \alpha_{sl,error} = 100\frac{W}{Km^2} \text{ (minimum uncertainty)} \tag{13}$$

$$\alpha_{sl,mean}^{outer} = ((100\frac{kW}{m^2K})^{-1} + (100\frac{W}{m^2K})^{-1})^{-1} = 50\frac{kW}{m^2K} \tag{14}$$

$$\alpha_{sl,lower}^{outer} = ((50\frac{kW}{m^2K})^{-1} + (100\frac{W}{m^2K})^{-1})^{-1} = 33\frac{kW}{m^2K} \tag{15}$$

for the outer target and

$$\alpha_{sl,upper}^{inner} = 27\frac{kW}{m^2K} \text{ (found experimentally as shown in Figure 7)} \tag{16}$$

$$\alpha_{sl,mean}^{inner} = ((27\frac{kW}{m^2K})^{-1} + (100\frac{kW}{m^2K})^{-1})^{-1} = 21\frac{kW}{m^2K} \tag{17}$$

$$\alpha_{sl,lower}^{inner} = ((21\frac{kW}{m^2K})^{-1} + (100\frac{kW}{m^2K})^{-1})^{-1} = 17\frac{kW}{m^2K} \tag{18}$$

for the inner target.

Although this seems to be a crude and unjustified attempt to resolve the difficulties introduced by co-deposited layers, the reader should note that the following section will

show that even if the values of q_{ELM}^{min} and q_{ELM}^{max} are strongly affected by the choice of α_{sl}^{inner}, this is not the case for the integrated energy over the period from $t_1 - t_4$. The above procedure was applied for each discharge within the data set. Since only comparable little variation has been found, the values for $\alpha_{sl}^{inner}$and $\alpha_{sl}^{outer}$are kept constant for all discussed discharges.

A much lower value for α_{sl}^{inner}has been found in comparison to α_{sl}^{outer}. This difference reflects the strong influence of surface layers on the inner divertor target on the thermography measurements. In contrast, a negligible influence at the outer target, consistent with this being a region of net erosion or balanced erosion/deposition, is found. This picture has been confirmed by a number of separate studies in JET [20, 32, 33] and, as mentioned earlier, is the result of a variety of complex physics processes involving both carbon chemistry, local transport processes in the divertor and plasma flows in the SOL [12, 34, 23, 35].

2.7. Effects of a non-zero surface layer heat capacity

Introducing a small, but finite heat capacity per surface area, β_{sl}, in the model, as attempted in [12], has no influence on the estimation of the deposited energy if the time interval used for the integration of the heat flux (and spatially integrated over the tile surface) is much larger than a characteristic time. This time, τ_{sl}, may be estimated according to:

$$\tau_{sl} = \frac{\beta_{sl}}{\alpha_{sl}} \tag{19}$$

where β_{sl} is estimated in equation 20 below [12]. At the inner target and for the experimental campaign in which the discharges discussed here were executed, post-mortem surface analysis found a layer thickness of $80\mu m$ and a 2 to 5 five times lower material density, ρ_{sl} for the surface layer than the CFC substrate material [20]. Assuming the layer density to be a factor 1/3 of that of the CFC substrate material and taking $\rho_{CFC} \cdot C_{CFC} = 3MJm^{-3}K^{-1}$ (see Table 3)

$$\beta_{sl} = \rho_{sl} \cdot C_{CFC} \cdot d_{layer} = \frac{1}{3} \cdot \rho_{CFC} \cdot C_{CFC} \cdot d_{layer} = 80Jm^{-2}K^{-1} \tag{20}$$

giving (using eqn.19) the following numerical value for τ_{sl}:

$$\tau_{sl} = \frac{\beta_{sl}}{\alpha_{sl}} = \frac{80Jm^{-2}K^{-1}}{17kWm^{-2}K^{-1}} = 4.7ms \tag{21}$$

The IR temperature signals during ELMs have been compared in [12] to divertor D_α emission. By adjusting the IR measured surface heat flux value such that it decays with the same slope as the divertor D_α signal, τ_{sl} was estimated at 5ms, in good agreement with the value derived in eqn. 21. More important for the analysis presented here is the comparison of the influence of the choice of τ_{sl} when applying integration intervals for 26ms $E_{t_1-t_4}$ and of 11ms giving $E_{t_1-t_3}$. Following the analysis in [12], the energy that is not accounted for through neglect of the surface layer heat capacity $\approx exp(-26ms/4.7ms) = 0.4\%$ for $E_{t_1-t_4}$ and $\approx exp(-11ms/4.7ms) = 10\%$ for $E_{t_1-t_3}$.

To compensate for this, the ELM target deposited energy ($E_{t_1-t_3}$) values presented in section 3 have been corrected ($1.1 \times E_{t_1-t_3}$) for the inner divertor. The same formalism for the outer divertor target with a layer thickness of $25\mu m$ [20], $\beta_{sl} = 25 Jm^{-2}K^{-1}$ and α_{sl}^{outer}=$33 kWm^{-2}K^{-1}$ gives $\tau_{sl} = 0.8ms$. The corresponding correction for the outer divertor can be therefore neglected since $exp(-11ms/0.8ms) \approx 10^{-6}$. The layer thickness was also estimated by post-mortem analysis.

2.8. Definiton of ELM target deposited energy E_{ELM}^{IR}

The temporally integrated power from time markers (t_1) to (t_3) in Figure 7 is denoted as $E_{t_1-t_3}$ and is an upper limit on the ELM target deposited energy.

$$E_{t_1-t_3} = \int_{t_1}^{t_3} P(t')dt' \tag{22}$$

The fraction of the inter-ELM energy that is simultaneously deposited in this time period cannot be precisely estimated using the available IR data. An approximation to an upper limit may, however, be derived assuming that the inter-ELM related power decreases linearly from the value at time marker (t_1) to that at time marker (t_3) such that the corresponding inter-ELM energy becomes

$$E_{t_1-t_3}^{corr} = \frac{1}{2} \cdot (P_{IR}(t_1) + P_{IR}(t_3)) \cdot (t_3 - t_1) \tag{23}$$

.

The value for the ELM deposited energy is, taking into account the latter inter-ELM related correction, then denoted by E_{ELM}^{IR} and is defined as follows:

$$E_{ELM}^{IR} = E_{t_1-t_3} - \frac{1}{2} \cdot E_{t_1-t_3}^{corr}. \tag{24}$$

where the factor 1/2 is chosen since $E_{t_1-t_3}^{corr}$ describes an upper limit and the real value is believed to be between this upper limit and zero.

Although the integration time in $E_{t_1-t_4}$ is larger as for $E_{t_1-t_3}$, the relative (and even the absolute) uncertainty of the estimated values of $E_{t_1-t_4}$ obtained by assuming different α_{sl} values is smaller than the correspodning α_{sl} dependent uncertainty of the values for $E_{t_1-t_3}$ as it can be verified in Table 4. This is because the choice of α_{sl} largely affects the heat flux values at the time (t_3) and only to a minor degree at (t_4). In order to estimate the resulting errorbar for $E_{t_1-t_3}$ explicitly due to this effect, the differences in the $E_{t_1-t_3}$ values found for different α_{sl} are used in the following way:

$$\Delta E_{t_1-t_3} = \sqrt{(E_{t_1-t_3}^{mean} - E_{t_1-t_3}^{upper})^2 + (E_{t_1-t_3}^{mean} - E_{t_1-t_3}^{lower})^2} \tag{25}$$

.

The resulting errorbar for E_{ELM}^{IR} is then given by

$$\frac{\Delta E_{ELM}^{IR}}{E_{ELM}^{IR}} = \sqrt{\left(\frac{\Delta E_{t_1-t_3}}{E_{t_1-t_3}}\right)^2 + \left(\frac{1/2 \cdot E_{t_1-t_3}^{corr}}{E_{t_1-t_3} - 1/2 \cdot E_{t_1-t_3}^{corr}}\right)^2} \tag{26}$$

accounting for the variation of $E_{t_1-t_3}$ with the choice of α_{sl} and the correction to the ELM energy, $E_{t_1-t_3}^{corr}$ due to the inter-ELM transport.

Table 5. Values for $E_{t_1-t_4}$, $E_{t_1-t_3}$, $1/2{\cdot}E^{corr}_{t_1-t_3}$ and E^{IR}_{ELM} for the assumed values for α^{inner}_{sl} and α^{outer}_{sl} for an arbitrarily chosen ELM in #53767 at $t = 23.7$ as marked in Figure 12 (b).

		inner		target		
α_{sl}	$E_{t_1-t_4}$	$E_{t_1-t_3}$	$1.1{\cdot}E_{t_1-t_3}$	$1/2{\cdot}E^{corr}_{t_1-t_3}$	E^{IR}_{ELM}	ΔE^{IR}_{ELM}
$\frac{kW}{m^2K}$	kJ	kJ	kJ	kJ	kJ	kJ
27	84.8	84.2	92.6	0.1	-	-
21	76.7	76.0	83.6	1.8	81.8	11.5
17	75.8	69.3	76.2	3.5	-	-
		outer		target		
α_{sl}	$E_{t_1-t_4}$	$E_{t_1-t_3}$	-	$1/2{\cdot}E^{corr}_{t_1-t_3}$	E^{IR}_{ELM}	ΔE^{IR}_{ELM}
$\frac{kW}{m^2K}$	kJ	kJ	-	kJ	kJ	kJ
100	122	83.9	-	26.1	-	-
50	121	78.9	-	27.3	53.9	27.7
33	118	74.6	-	27.5	-	-

Table 5 presents the values for $E_{t_1-t_4}$, $E_{t_1-t_3}$ ($1.1{\times}E_{t_1-t_3}$ for inner only), $E^{corr}_{t_1-t_3}$ and E^{IR}_{ELM} for an arbitrarily chosen ELM from discharge # 53767 at t=23.7 seconds for all used values of α^{outer}_{sl} and α^{inner}_{sl}. This time is within the temporal period chosen for the later analysis. Owing to its small size in comparison with $E_{t_1-t_3}$, the variation of $E^{corr}_{t_1-t_3}$ due to different choices of α_{sl} is not accounted for. The result for this particular ELM is also marked in Figure 12 (b). It should be noted that the data shown in Figure 7 and Table 4 correspond to a sooner time period within the same discharge but when the inner divertor is (still) power attached which makes the presentation of the $E^{corr}_{t_1-t_3}$ value illustrative.

The value and errorbar for the inter-ELM transport are derived by using the integrated energy for the full discharge using equation 8 with $t = t_{end} = 30s$ defining the end of each discharge and subtracting the energy for all ELMs within this time interval as defined by equation 24:

$$E_{inter-ELM} = E(t_{end}) - \sum_{i}^{n} E^{IR}_{i,ELM} \tag{27}$$

$$\Delta E_{inter-ELM} = \frac{1}{n} \sum_{i}^{n} \Delta E^{IR}_{i,ELM} \tag{28}$$

with n as the total number of ELMs in the chosen time window.

2.9. Comparison with thermocouple energies and energy entering the SOL

Figure 8 (a) compares the deposited energies per discharge derived from IR measurements and with tile embedded thermocouples (TC) according to the technique developed in [36]. In both cases, analysis is restricted to the target tiles #3 and #7 (locations of the strike zones as illustrated in Figure 1). The IR analysis yields in average slightly higher energies for the inner target and slightly lower for the outer

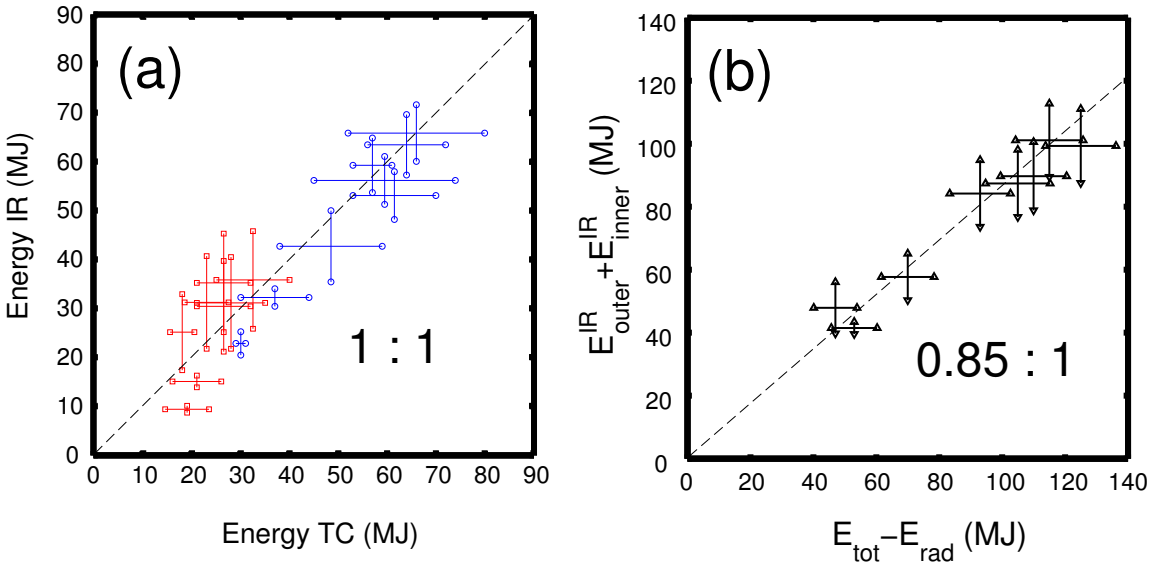

Figure 8. Comparison of (a) energy deposited on tiles #3 (red squares) and #7 (blue circles) measured by IR thermography with that deduced from analysis of tile thermocouples for the discharges in Table 1 and (b) total IR measured energy (tile #3 and #7) for 8 ELMy H-Mode plasmas. The quantity (E_{tot} -E_{rad}) is the energy conducted and convected into the SOL.

target compared with the thermocouple data, but agreement is generally good. In Figure 8(b), the IR data validation is extended to a comparison between the integrated total tile energy and that conducted and convected into the SOL, E_{tot} -E_{rad} . The quantity E_{rad} denotes the energy radiated by the plasma, E_{tot} the total energy for plasma heating (ohmic + additional), and E_{IR} is the total deposited energy on the divertor targets. Roughly 85% of E_{tot} -E_{rad} is observed to arise at the divertor strike zones in fair agreement to earler studies [6]. The remaining energy is thought to be deposited on the main chamber walls by ELM and inter-ELM convective radial transport [37, 25] or by charge-exchange losses [38].

In this energy balance analysis, corrections due to the deposition of radiated energy onto the divertor target tiles, which are considerable for highly radiating divertor plasmas, have not been accounted for. A careful balance has been performed for discharge #53772, which employed nitrogen seeding for ELM mitigation studies using high radiation [39]. In this case, the balance does account for radiation onto the target plates. The result demonstrates that the error involved in not accounting for the radiation amounts to no more than 10-15% except during transitions from low to high confinement and vice versa, where errorbars can exceed 30%. This effect is not attributed to the deposition of radiation on the divertor, but to uncertainties in the rate of change of the plasma stored energy and the resulting accuracy of dE_{plasma}/dt during the transition.

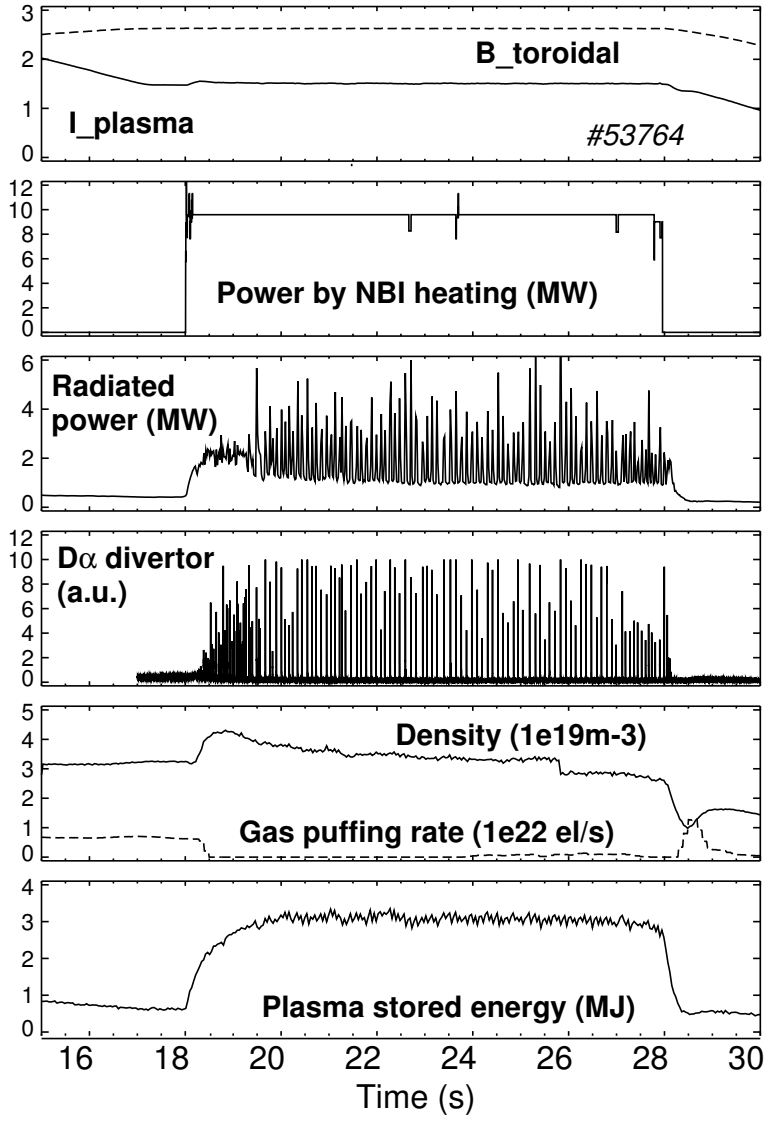

Figure 9. Time evolution of the main plasma parameters in the IR-optimised discharge # 53764.

3. Results

Figure 9 illustrates the temporal evolution of the main plasma parameters for discharge # 53764 and will be used as an additional example of the analysis performed for the set of IR-optimised discharges. This discharge complements #53767 (see Figure 2) in two respects: both divertor legs are power attached due to the relatively low plasma density and the ELM frequency is relatively low (around 11Hz) and very regular, so that both ELM and inter-ELM transport can be investigated in detail. All other deuterium discharges (#53765,#53767,#53768,#53770, see Table 1) have higher plasma current (2.5MA) and hence higher plasma densities, particularly after the gas puffing phase, pushing the inner divertor to detachment or close to detachment.

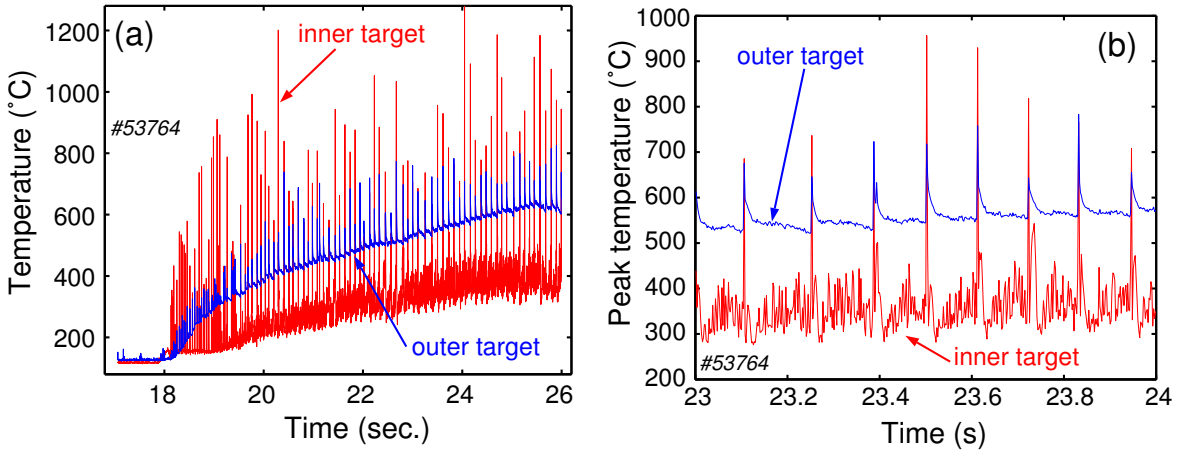

Figure 10. Time evolution of the maximum temperature on the inner (tile #3) and outer (tile #7) target tiles in discharge #53764 for (a) the diverted phases of discharge and (b) a time window of one second during the steady-state phase of the heating and fuelling waveforms.

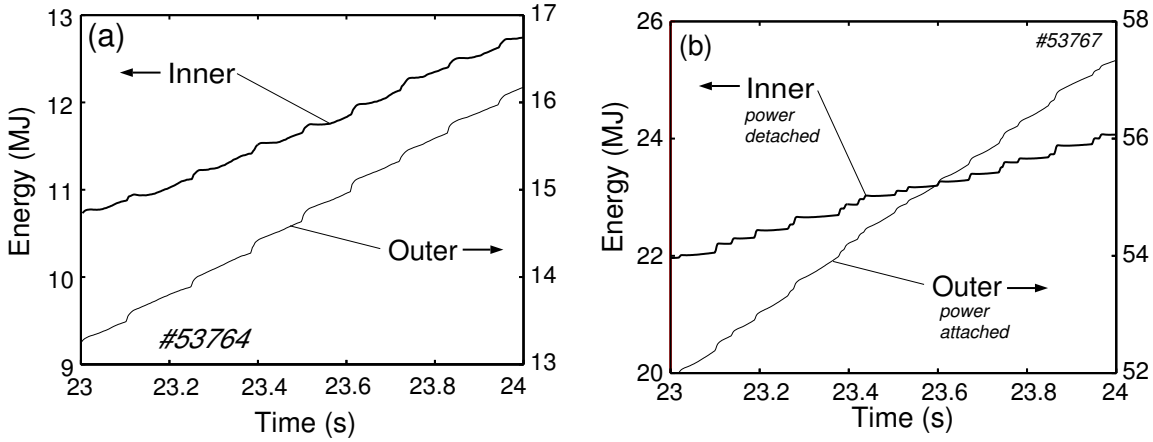

Figure 11. Temporal evolution of the divertor target deposited energies during a 1 second phase of (a) discharge #53764 and (b) #53767.

3.1. Evolution of temperature, power and energy

The time evolution of the IR measured surface temperature on the outboard/inboard targets is shown in Figure 10(a) for the diverted phase of the discharge and in Figure 10(b) for a shorter time window of 1 second. Evidently, the maximum surface temperatures, T^{max}_{inner} , T^{max}_{outer} , on both the inner and outer divertor targets increase monotonically throughout the discharge in-between ELMs. It is also clear that T^{max}_{outer} varies smoothly both in-between ELMs and during the temperature decay following an ELM, while T^{max}_{inner} varies erratically in a range of $\approx 100^oC$ in-between ELMs. The comparison of T^{max}_{outer} and T^{max}_{inner} during the ohmic phase of the discharge, where both targets have similar low temperature values, demonstrates that the inner target behaviour cannot be ascribed to a systematic diagnostic error.

During the ELM power deposition phase, both T^{max}_{inner} and T^{max}_{outer} increase strongly,

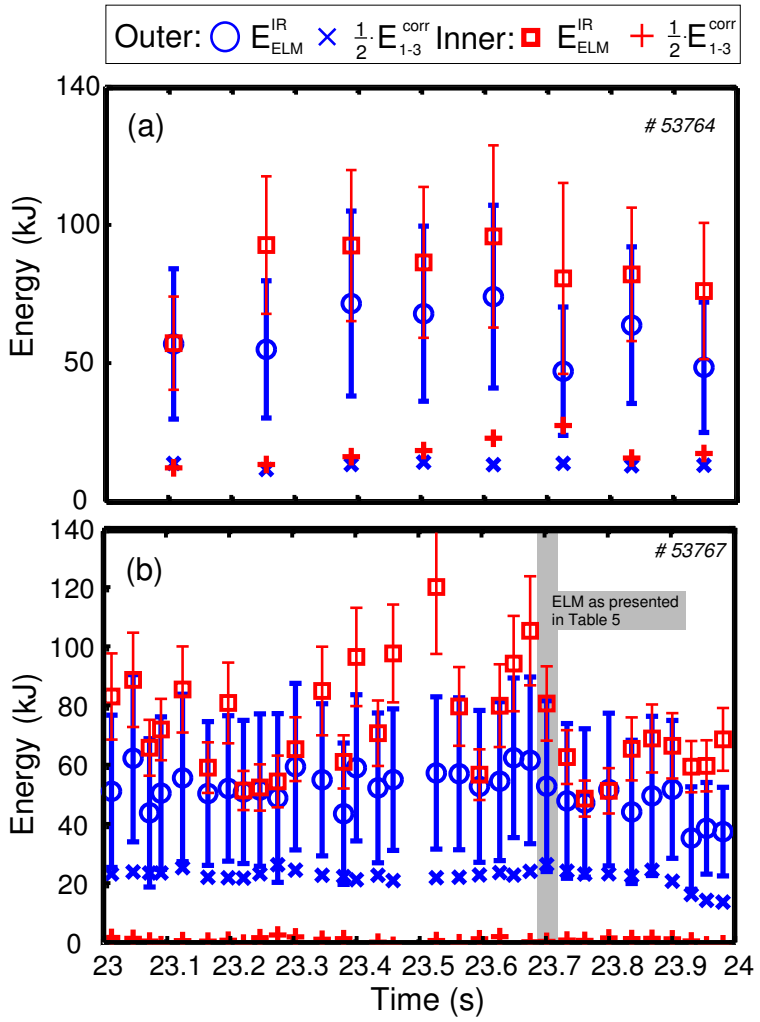

Figure 12. The ELM deposited energy, E^{IR}_{ELM} , is estimated by integrating the power deposition around the ELM peak power flux as shown here for (a) #53764 and (b) #53767 including the correction energy, $E^{corr}_{t_1-t_3}$, due to the inter-ELM transport.

with maximum temperatures at the inner target exceeding those at the outer target. Although these observations would appear to indicate that a higher heat flux is deposited at the inner divertor during ELMs, the larger temperature rise on the inner divertor target is mainly due to the influence of co-deposited surface layers on the IR measurements.

Calculated divertor deposited energies for a discharge with low and high I_p are shown in Figure 11 (a,b) respectively. In discharge #53764 (low I_p), most of the energy arrives at the targets predominantly in-between ELMs. In contrast, for pulse #53767, with highest n_{av} and I_p in the set of discharges studied here, the ELMs are the largest contributors to the inner target energy load, with the outer target energy deposition still dominated by the inter-ELM periods. This is due to the strong reduction in inter-ELM energy deposition associated with inner divertor detachment. As a consequence, as shown in Figure 11(b), the deposited energy on the inner target increases in time

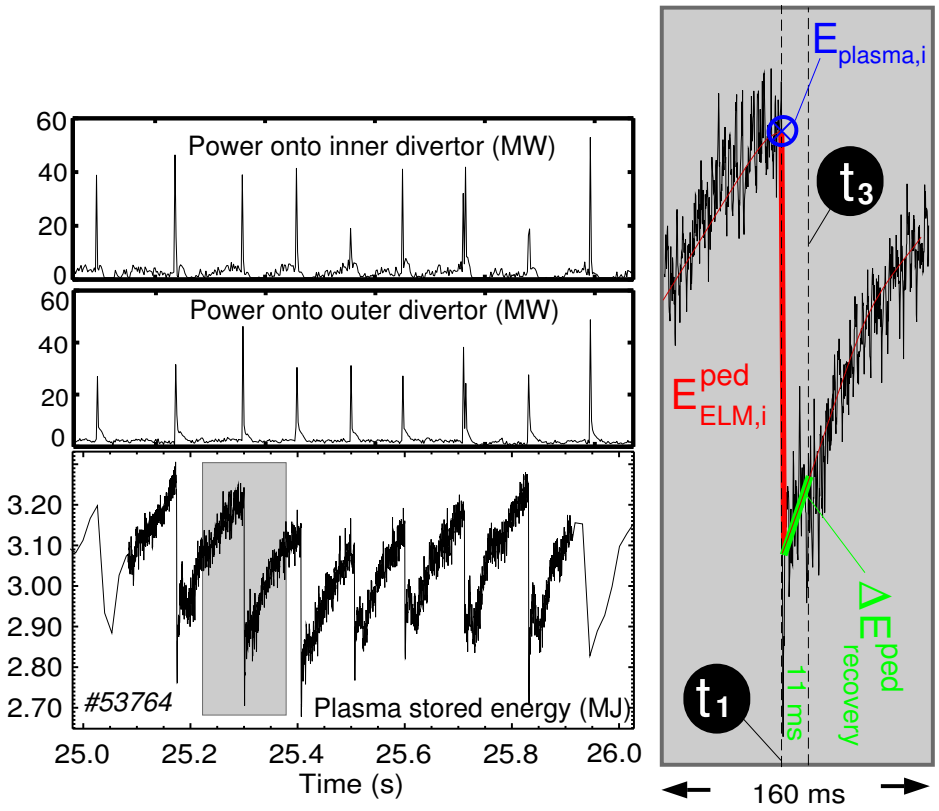

Figure 13. Power deposited at the inner and outer targets and plasma stored energy during a short period in discharge #53764. The drop of plasma stored energy during Type-I ELMs causes the power increases measured at the divertor target.

in a stepwise manner, with each step caused by a single ELM. This is consistent with the inner divertor being detached in the inter-ELM phases and re-attaching during the ELM phases [40].

Figure 12 shows the temporal evolution of the ELM energies E_{ELM}^{IR} and corrections, as defined in section 2.8, for both discharges in Figure 11. In case (a), where both strike points are power attached throughout the diverted discharge phase, a slightly higher fraction of ELM energy is found at the inner target than at the outer target. The energy, $E_{t_1-t_3}^{corr}$, reflecting the uncertainty of the inter-ELM transport during the ELM event is roughly equal for both divertor targets. For the case in (b), in which the inner divertor leg is mainly detached the ELM energy correction for the inner divertor is consequently found to be approximately zero. The ELM energy deposition ratio is similar to the one from case (a) with a slightly larger ELM energy on the inner divertor.

3.2. Comparison of target and pedestal loss ELM energies

The values of the power reaching the inner and outer divertor target for discharge #53764 are shown in Figure 13, together with the evolution of the complete plasma stored energy. It has been shown in various contributions from several experiments that the ELM caused plasma energy loss is mainly affecting the pedestal region[30, 41, 42, 43].

Therefore, the ELM caused energy loss is named E_{ELM}^{ped} . In order to calculate the fraction between the plasma energy drop caused by Type-I ELMs and resulting energy fluxes onto the target plates at each event, the values for E_{ELM}^{ped} are derived as illustrated in the right box of Figure 13 and averaged to a single value:

$$E_{ELM}^{ped} = \frac{1}{n}\sum_{i}^{n} E_{ELM,i}^{ped} \tag{29}$$

In order to estimate the errorbar of the latter quantity the reader should recall that in equation 24 the calculation of the ELM deposited target energy takes into account the time intervall from t_1 to t_3 giving $E_{t_1-t_3}$ and is including also the correction due to the inter-ELM energy $-1/2\times$ $E_{t_1-t_3}$. In other words, by introducing a surface layer correction the errorbar of E_{ELM}^{ped} should include the power crossing the separatrix within the time $t_3 - t_1 = 11ms$. Given the comparable crude time resolution of the radiated power, P_{rad} , of only 20ms the radiation is here completely ignored. A reasonable expression for an upper limit of power crossing the separatrix is then taken into account by

$$P_{separatrix} = P_{NBI} - dE_{plasma}/dt \tag{30}$$

Integrating the power crossing the separatrix from t_1 and t_3 the corresponding errorbar for E_{ELM}^{ped} is calculated according to

$$\Delta E_{t_1-t_3}^{separatrix} = \int_{t_1}^{t_3} (P_{NBI})dt' - \Delta E_{recovery}^{ped} \tag{31}$$

. For the presented example in Figure 13 with $\Delta E_{recovery}^{ped}\approx$ 50kJ and P_{NBI} =9.5MW, $\Delta E_{t_1-t_3}^{separatrix}$ is found to be 55kJ and therefore a comparable small correction to the value for E_{ELM}^{ped} of 342kJ for the given example. However, this correction is included in the errorbar estimation. Additionally to the latter errorbar the statistic variation of the single E_{ELM}^{ped} values is taken into account leading finally to

$$\Delta E_{ELM}^{ped} = \frac{1}{n}\sqrt{\sum_{i}^{n}\{(E_{ELM,i}^{ped} - E_{ELM}^{ped})^2 + (\Delta E_{t_1-t_3,i}^{separatrix})^2\}} \tag{32}$$

providing the errorbar as used for the pedestal energy loss during type-I ELMs here.

To compare different experiments commonly the latter value is normalized either to the overall or the pedestal stored energy. The ELM energy loss, as stated above, is observed to origin in the pedestal region and therefore a normalization to the pedestal stored energy is preferred. Moreover, varying pressure profile characteristics potentially [44] result in different ratios between overall and pedestal stored energy and are excluded this way. However, for the given discharges in JET with relatively low triangularity and small variation of the latter value the ratio between pedestal stored energy and overall plasma stored energy is assumed to be $\approx 0.33\pm 0.03$. This value of pedestal to total energy ratio is consistent with a wide database of JET measurements for these triangularities [29]. By taking the value for the plasma energy, E_{plasma} just before the ELM crash as illustrated in Figure 13, the pedestal stored energy, E_{ped} , can be

approximated as:

$$E_{plasma} = \frac{1}{n}\sum_{i}^{n} E_{plasma,i} \tag{33}$$

$$\Delta E_{plasma} = \frac{1}{n}\sqrt{\sum_{i}^{n}(E_{plasma,i} - E_{plasma})^2} \tag{34}$$

$$E_{ped} = 0.33 \times E_{plasma} \tag{35}$$

$$\Delta E_{ped} = \sqrt{(0.33 \cdot \Delta E_{plasma})^2 + (0.03 \times E_{plasma})^2} \tag{36}$$

Figure 14 compares the ELM energy deposited at the targets (E_{ELM}^{IR}) normalised to the energy lost from the pedestal (E_{ELM}^{ped}) and the energy lost from the pedestal (E_{ELM}^{ped}) normalised to the pedestal plasma energy (E_{ped}). The errorbar for the ratios between E_{ELM}^{IR} and E_{ELM}^{ped} and between E_{ELM}^{ped} and E_{ped} are again calculated by making use of the standard error propagation formalism.

A few older data points are also included in Figure 14 drawn from a previous publication[2]. They were obtained on the basis of fast ELM averaging[17], without accurate estimation of the inter-ELM corrections and using slightly different assumptions for processing of the pedestal top parameters. The main difference between both data sets is found in the slightly lower values for E_{ELM}^{IR} due to the inter-ELM transport correction ($E_{t_1-t_3}^{corr}$), but otherwise no qualitative differences are evident. The fraction of ELM energy arriving at the divertor $E_{ELM}^{IR}/E_{ELM}^{ped}$ appears to be ≈ 0.75 for values of $E_{ELM}^{ped}/E_{ped} \approx 0.15$ (small ELMs) decreasing to $E_{ELM}^{IR}/E_{ELM}^{ped} \approx 0.45$ for values of $E_{ELM}^{ped}/E_{ped} \approx 0.3$ (large ELMs). Even a systematic variation of all data points underestimating the values for E_{ELM}^{IR} or overestimating E_{ELM}^{ped} cannot exceed the true value by more than 25% since adding the latter value to E_{ELM}^{IR} (or subtracting it from E_{ELM}^{ped}) for smallest ELMs in the data set would give the full pedestal loss energy deposited on the targets (i.e. $E_{ELM}^{IR}/E_{ELM}^{ped}$ =100%). Even then, the obvious trend from Figure 14 showing larger ELMs to deposite a smaller fraction of the pedestal loss energy than smaller ELMs still holds true. Therefore, and thanks to the careful calibration of the IR camera for largest observed temperatures as discussed in section 2.9, the data in presented in Figure 14 demonstrate that larger ELMs tend to deposit a lower fraction of the pedestal loss energy onto the divertor target plates.

3.3. ELM and inter-ELM energy and power

Figure 15 (a) shows the Greenwald density fraction for each time window of the discharges under consideration here versus the pedestal collisionality in order to give a crude characterisation of these discharges. ELMs are triggered by MHD instabilities at the plasma edge, which are believed to be driven by pressure and edge current gradients, associated with the edge transport barrier in H-modes [45]. In particular, the edge current is driven by the bootstrap current, which is influenced by plasma collisionality with lower bootstrap currents at higher plasma collisionalities. Therefore, it has been proposed that ELM energy losses can be influenced by edge plasma collisionality. Inter-

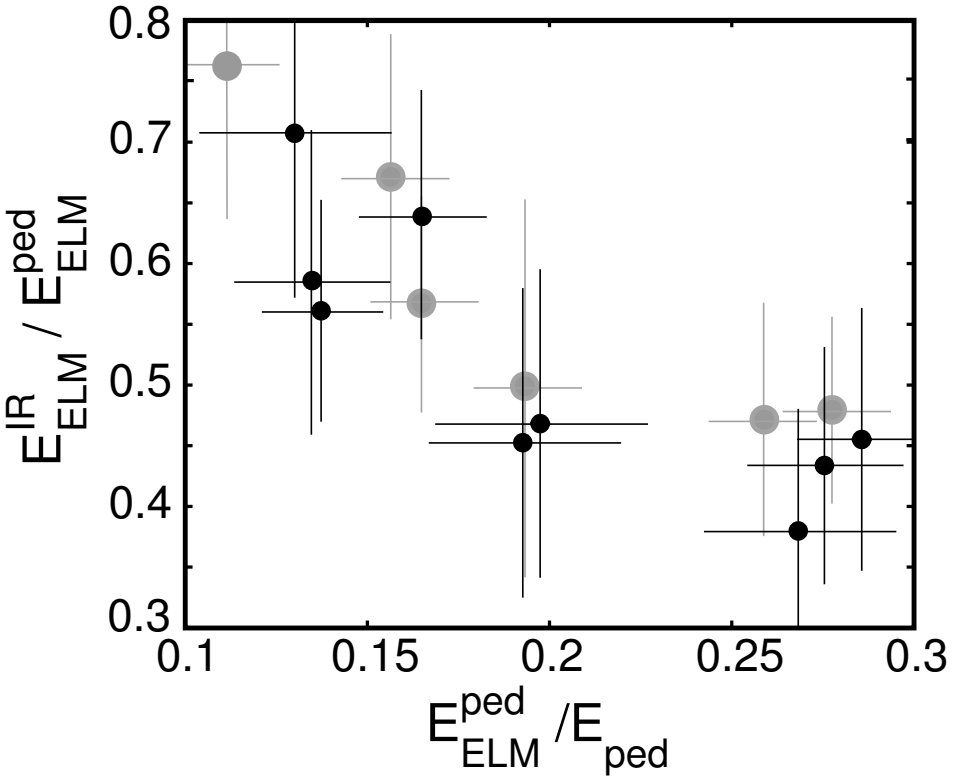

Figure 14. Measured ratio of, ELM target, E^{IR}_{ELM} to ELM pedestal loss energy, E^{ped}_{ELM} versus normalised ELM size defined as E^{ped}_{ELM} $/E_{ped}$ as black data points. The grey shaded data points correspond to older results ([2]).

machine energy losses comparisons of the normalised ELM energy losses from most tokamaks have indeed demonstrated that the plasma collisionality of the pedestal is a major factor determining the actual amount of energy lost at the ELMs, see e.g.[46]. The collisionality of the pedestal plasma is calculated according to the neoclassical formula as given by

$$\nu^*_{ped} = R \times q_{95} \times \epsilon^{-3/2} \times \lambda^{-1}_{e,e} \tag{37}$$

, where $\lambda_{e,e}$ is the electron-electron coulomb collision mean free path, $\epsilon = a/R$ and $\lambda_{e,e} = 1.727 \cdot 10^{17} T(eV)^2/n(m^{-3})/\ln(\Lambda)$ with $\ln(\Lambda) = 13$. The quantities n_{ped} and T_{ped} describe the density and temperature at the top of the H-Mode pedestal, respectively. The Greenwald density fraction is defined as

$$\text{Greenwald density fraction} = n_{av}(10^{20} m^{-3}) \cdot \frac{\pi a(m)^2}{I_p(MA)} \tag{38}$$

with $a = 0.9m$ and $R = 3.8m$ for the analysed discharges.

Figure 15 (b) shows the ELM pedestal loss energy which in average decreases with higher $\nu^*_{\rm ped}$ values but also shows a large scatter of the single data points varying between 200kJ and 500kJ. Figure 15 (c) shows the ELM target deposited energy varying between 120kJ and 200kJ, so showing a reduced variation than the ELM pedestal loss energies. Finally Figure 15 (d) shows the deposited energy between two consecutive typical ELM

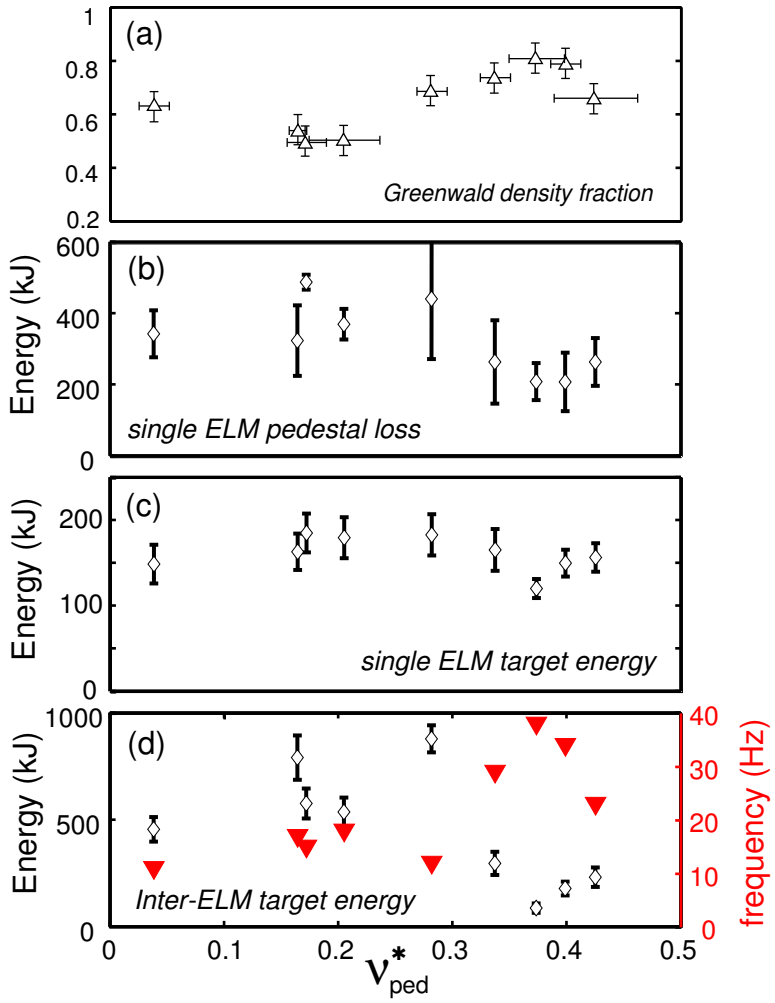

Figure 15. The (a) Greenwald density fraction and (b) pedestal loss energy of a typical ELM event, (c) target deposited energy of a typical ELM event and (d) target deposited energy between two ELM events together with the ELM frequncies.

events which are largely varying due to the variation of the ELM frequencies which are presented in the same plot. With higher $\nu^*_{\rm ped}$ values the ELM frequency increases in average but also here a large scatter is observed. This effect is possibly caused by the different triangularity in these discharges which is reported to cause a significant additional varitation of the relation between the normalised ELM pedestal loss and ELM frequency or $\nu^*_{\rm ped}$ [47, 48].

Figure 16 shows the ELM transported power across the separatrix and onto the targets in (a) and (b), respectively. Both quantities increase with higher $\nu^*_{\rm ped}$ values. The inter-ELM power shown in (c) drops significantly at large $\nu^*_{\rm ped}$. The total power enntering the SOL, P_{tot} -P_{rad} , stays relatively constant as shown in (d). Additionally the power balance between the former value and the deposited energy, P_{tot} -P_{rad} -P_{IR} , is presented, confirming that no systematic ($\nu^*_{\rm ped}$ dependent) errorbar is present in the data supporting the results of Section 2.9.

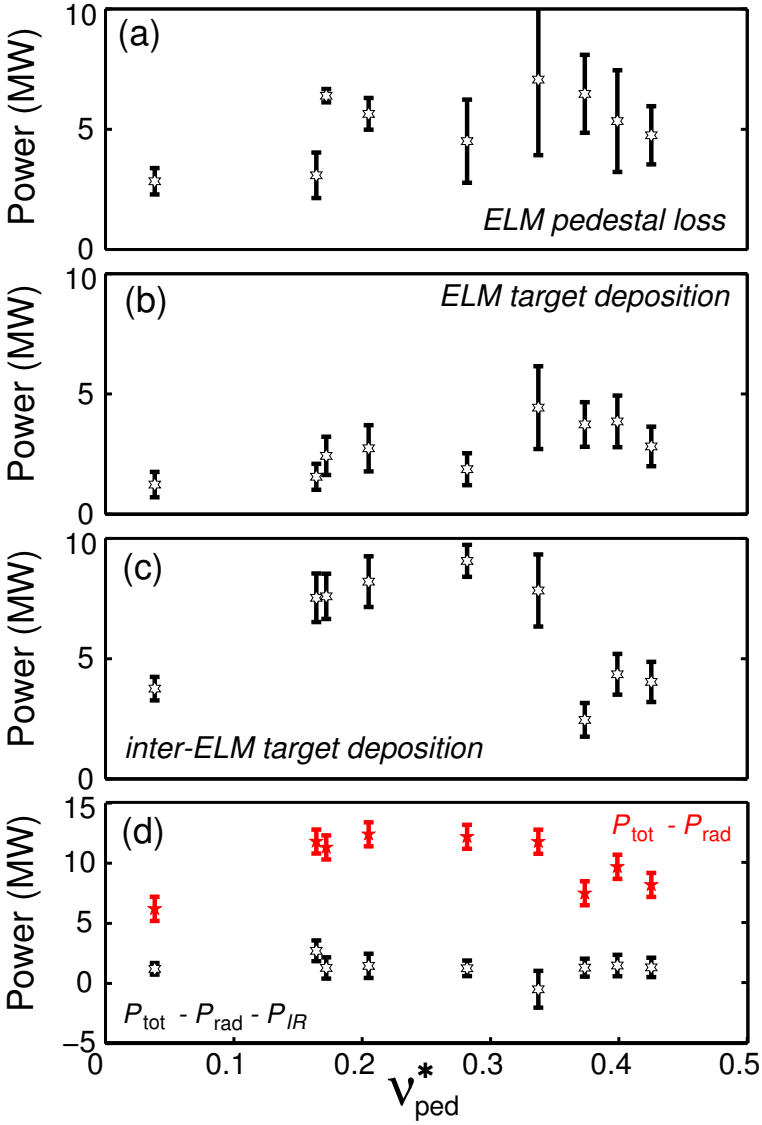

Figure 16. The (a) power transported across the separatrix due to ELMs, (b) power deposited onto the targets due to ELMs, (c) inter-ELM target power deposition. (d) presents (red data points) P_{tot} -P_{rad} and (black data points) the power balance between the former quantity and the power found on the divertor target plates, P_{tot} -P_{rad} -P_{IR} .

3.4. Target energy deposition in/out asymmetry

Figure 17 shows the pedestal collisionality dependence, $\nu^*_{\rm ped}$, of the in/out energy deposition ratio for (a) during the ELM, (b) inter-ELM period and (c) ELM-averaged for the discharge phases defined in Table 1. The in/out deposited energy ratio for individual ELMs remains rather constant across the whole collisionality range, increasing slightly with pedestal collisionality from values close to unity to values $\approx$ 1.5:1 with the exception of the data point with the lowest $\nu^*_{\rm ped}$ in the whole data set. Inner divertor detachment clearly, therefore, has no mitigating effect on the magnitude of the ELM energy deposition onto the inner divertor. The inter-ELM ratio shows similar values to

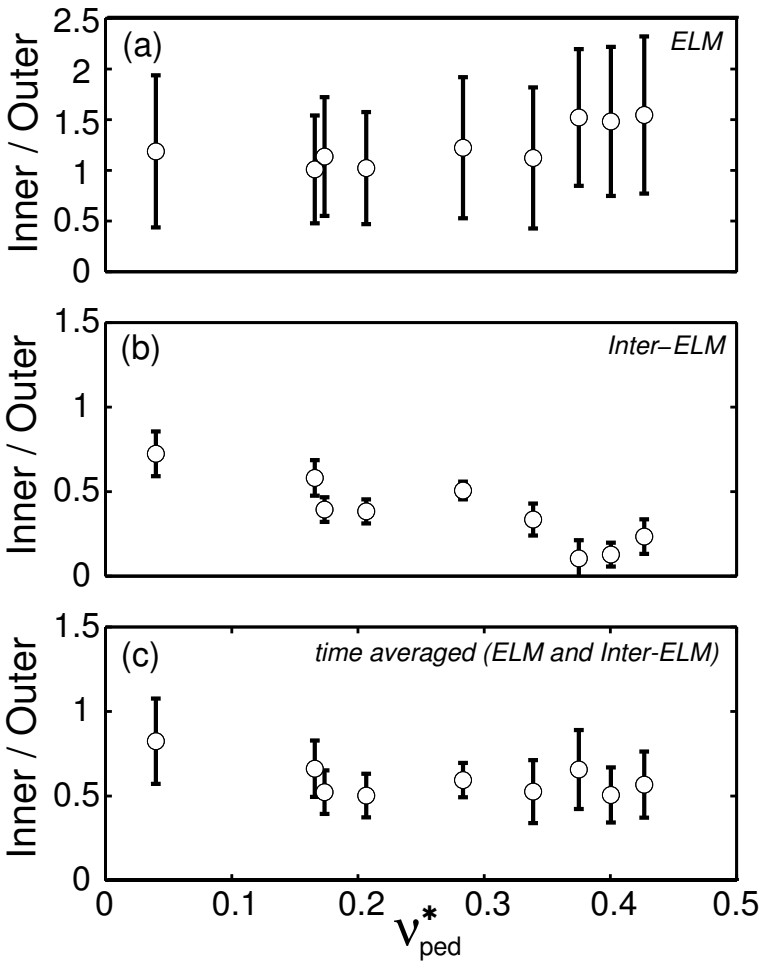

Figure 17. Ratio between outer and inner divertor target deposited energy for (a) ELM events, (b) inter-ELM and (c) time averaged about ELMs and Inter-ELM periods versus the pedestal collisionality in the corresponding phase of the discharge.

the ELM-averaged value only at low $\nu^*_{\rm ped}$, but for $\nu^*_{\rm ped} \geq 0.3$ decreases to lower values close to zero as the inner divertor plasma detaches. Whilst the inter-ELM transport and time-averaged (including ELMs and Inter-ELM periods) transport clearly favours the outer target, as expected from classical drifts, ballooning transport and (due to the Shafranov-Shift) toroidal geometry (see e.g. [23, 49, 50]), the ELM transport appear to drives a higher fraction of the energy towards the inner divertor. The ELM-averaged in/out ratio displays no systematic variation with the pedestal collisionality, distributing around values of ≈ 0.55. This value is found to be in rough agreement to studies based on thermo couples alone (therefore not ELM resolved) reporting values of ≈ 0.45[23].

3.5. Fraction of ELM to overall divertor deposited energy

Figure 18 shows the ratio between the ELM deposited energies and overall target deposited energy for (a) the outer and inner targets taken together, (b) the outer target and (c) the inner target only versus $\nu^*_{\rm ped}$. For the inner divertor divertor target the

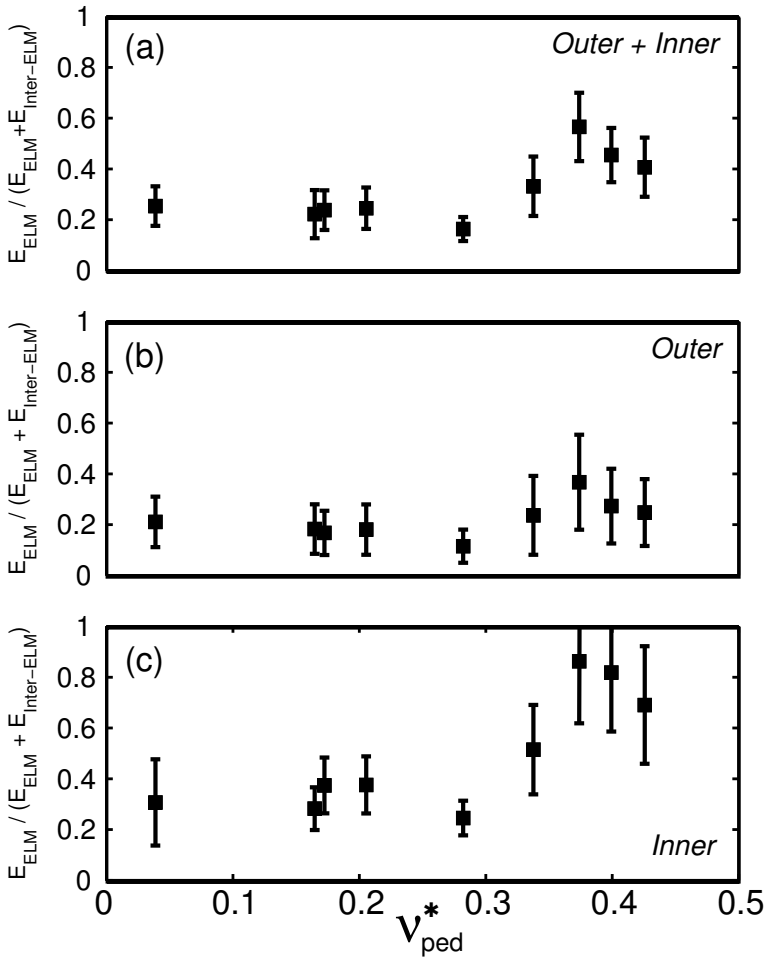

Figure 18. Ratio between ELM and inter-ELM divertor deposited energies for (a) outer + inner target, (b) outer and (c) inner target versus the pedestal collisionality.

fraction of energy carried by ELMs increases strongly with higher $\nu^*_{\rm ped}$ values, whereas it incraeses only very slightly for the outer divertor. This behaviour is well understood for the inner divertor, since the inter-ELM energy essentially starts to disappear at the onset of partial plasma detachment[40]. At this point, the deposited energy is due to the ELMs becomes more important and at highest $\nu^*_{\rm ped}$ values in the data set the deposited energy is nearly completely due to ELMs.

Taking both targets together it is found that at the highest $\nu^*_{\rm ped}$ values the ELM energy deposition fraction is equal to the Inter-ELM energy deposition whereas at lower $\nu^*_{\rm ped}$ values the inter-ELM fraction is the dominant energy deposition channel onto the divertor targets.

Significant detachment for the outboard divertor is never in practice obtained in JET Type-I ELMy H-mode discharges, consistent with the weak dependence on $\nu^*_{\rm ped}$ of the outer ELM energy fraction carried to the outer target. However, an effect due to weak partial detachment for the outer divertor can not be excluded in the high density phases analysed here.

To which extend the observed behaviour is caused by a change of ELM energy loss characteristic from the pedestal region and SOL transport at high density or by the divertor conditions at high densities cannot be resolved using this restricted data base. Independently of the exact cause of this behaviour, these JET results demonstrate for the inner divertor that the power deposition balance at higher $\nu^*_{\rm ped}$ is dominated by ELMs and by the inter-ELM transport at low $\nu^*_{\rm ped}$. For the outer divertor these results demonstrate that for all values of $\nu^*_{\rm ped}$ in the data set the inter-ELM transport is the dominant fraction.

4. Discussion

They are three notable aspects of the analysis presented here which are discussed in the following:

(1) The fraction of ELM to inter-ELM deposited energy

(2) The asymmetry between inner and outer ELM energy deposition

(3) The fraction of ELM energy arriving at the divertor target

(1) The fraction of the ELM to inter-ELM divertor target deposited energy shows for low $\nu^*_{\rm ped}$ values of around 0.25. For higher values of $\nu^*_{\rm ped}$, and correspondingly higher ELM frequencies, a larger ELM carried energy fraction up to ≈ 0.5 is found. This behaviour is well explained by the content of the paper. First, the fraction between ELM loss and target deposited energy is higher for (smaller) ELMs appearing at higher $\nu^*_{\rm ped}$ values. Second, the inter-ELM target deposition onto the inner divertor is largely reduced when inner divertor target power detachment sets in whereas significant detachment of the ELM inner target deposition is not observed.

(2) One striking feature of the type-I ELM energy target deposition is the larger fraction of energy deposited onto the inner divertor target than on the outer target. Careful estimation of diagnostical errorbars, particularly due to the presence of surface films on the divertor targets, has been presented and are taken into account. Indeed, given the large resulting errorbars in/out ratios of the target deposition below unity would be possible. However, recent results from ASDEX Upgrade infra-red thermography for the upper divertor, making use of an optimised experimental setup to avoid influences of co-deposited surface layers, also show that the ELMs deposit more energy onto the inner divertor [25, 51]. These results were obtained for the same field direction (normal field direction) as it was applied in the JET discharges under consideration here. For reversed field direction it was shown, that ELMs drive a higher fraction towards the outer divertor target[51]. The latter work includes target current measurements j_0 using shunts measuring the currents between the target tiles and earth and showing a clear correlation between the measured energy asymmetry and the amplitude of the j_0 signal. To envisage this specific point in JET a benchmark of the results on the ELM target energy distribution as presented here and j_0 and j_{SAT}

measurements are in progress. For a discussion about the possible underlying phycial mechansim see also [51].

(3) The values found for the deposited fraction of ELM energy compared to the pedestal loss and thus energy crossing the separatrix are similar to the values found when the divertor ELM-average power is normalised to the additional heating power (see the column in Table 1 giving P_{IR}/P_{NBI}). Under steady-state conditions, the difference between the measured IR deposited power and the additional heating power can be explained by the power radiated electromagnetically from the plasma. Measurements of plasma radiation in JET are too slow to determine whether the difference between ELM pedestal loss energy and target energy can be accounted for by ELM-induced radiation. However, results are available which indicate that only a small fraction of the ELM pedestal loss energy is radiated in JET.

For nitrogen seeding experiments with resulting very small Type-III ELMs with an energy pedestal loss of less than 20kJ resulted in a complete dissipation of ELM (and inter-ELM) energy [39, 52]. In contrast, for cases with Argon seeding and Type-I ELMs of the size of a few hundreds kJ no significant increase of the radiation level has been reported compared to unseeded discharges [53]. JET modelling on the feasibility of ELM energy dissipation in the SOL using impurity seeding techniques has shown that higher impurity content barely increases the radiated ELM energy fraction and that the relative fraction of radiated energy during the ELM is less than 10% for ELMs larger than 100kJ [54]. These results are consistent with modelling studies for ITER, which predict negligible ELM radiation fractions for Type-I ELMs [55]. Assuming therefore an ELM provoked radiation level not exceeding 10% in the analysed discharges, the IR thermography data imply that up to 45% of the pedestal energy for very large ELMs could be deposited remote from the strike lines (tile #3 and #7) with a significant fraction deposited onto the main chamber walls.

Experimental evidence is reported in [56] from JET discharges for peak ion temperatures in ELM filaments reaching the main chamber walls in the range of 50% of the pedestal values. These latter experimental results are in good agreement to the transient model of ELM energy dissipation to radial parallel losses [57]. This model makes use of measured values for the ELM radial propagation velocity, $v_\perp$, performed by first wall limiter target mounted Langmuir probes located at several poloidal positions in the outer equatorial midplane region providing several radial distances between the probe tips and the pre-ELM separatrix location [58]. Measurements from a single reciprocating probe located also at the outer midplane [59] finds the ELM radial propagation speed to increase roughly linear with the numbers of ELM related particles arriving at the probe. Based on the latter finding and assuming that the number of particles and the energy pedestal loss is positively correlated, it gets clear that larger ELMs will deposit less of their energy onto the divertor target tiles and more to the wall since they travel faster across the SOL than smaller ELMs. However, experimental findings showing correlations between the ELM energy loss size and $v_\perp$ is not yet reported from JET.

Instead, in a notably simple attempt to derive the energy fraction to the first wall in JET (and ITER) an empirical scaling is developed [60] and will be compared in the following to the results found here. In the latter work a midplane power decay length for ELMs in the far SOL is estimated for medium sized ELMs (E^{ped}_{ELM} / $E_{ped} \approx 0.12$) by experimentally changing the plasma-wall gap in JET DOCL discharges [29] and found to be $\lambda^0_{ELM} \approx 3.5$cm. The dependence of λ_{ELM} on the ELM size is then assumed to scale as

$$\lambda_{ELM} = \lambda^0_{ELM} \cdot \left[\frac{E^{ped}_{ELM}}{E_{ped} \cdot 0.12}\right]^{\chi} \tag{39}$$

Since the decay length can be generally related to the radial and parallel transport velocities (or times)

$$\lambda_{ELM} \sim v_{\perp}/c_s \cdot L_{||} \tag{40}$$

this ansatz also provides in return a scaling of the dependence of $v_{\perp}$ on the ELM size (E^{ped}_{ELM} /E_{ped}), see also e.g. [61]. In other words, in equation (39) the quantity χ reflects the dependence of $v_{\perp}$ /c_s on the relative ELM size with c_s being the parallel ion sound speed and $L_{||}$ an average connection length in the SOL region during the ELM.

The energy fraction deposited to the wall elements is then simply calculated as

$$f_{wall} = \frac{E^{Wall}_{ELM}}{E^{ped}_{ELM}} = \exp(-\Delta^{ELM}_{Wall}/\lambda_{ELM}) \tag{41}$$

The distance of the pre-ELM separatrix to the wall is given by $\Delta_{Wall} = 4.5cm$. The target tiles under consideration here, tile #3 and tile #7, correspond to a radial distance, Δ_{IR}, from the pre-ELM separatrix into the SOL of about 1.5cm. The field lines between Δ_{IR} and Δ_{Wall} end on the tile #1 (far SOL inner) and tile #8 (far SOL outer), see Figure 1. Unfortunately tile #1 is not covered by the IR camera view so that the analysis can be extended towards this tile. To compensate for this, the energies accumulated during the entire discharge as measured by thermocouples are used and it is assumed that the ELM carried fraction of energy deposited onto targets #1 and #8 are the same as for tile #3 and #7. For the first wall no experimental data can be derived using the infra-red thermography system as described here. The values for Δ_{IR} and Δ_{Wall} have been derived by using magnetic reconstruction before the ELM event. Therefore, the ELM event instability process itself imposes an intrincic uncertainty for Δ_{IR} and Δ_{Wall} which is in the following denoted as Δ_{ELM}. Expressing this intrinsic uncertainty in a highly simplified way as

$$\Delta^{ELM}_{Wall} = \Delta_{Wall} + \Delta_{ELM} \tag{42}$$

equation (41) can be rewritten as

$$f_{wall} = \frac{E^{Wall}_{ELM}}{E^{ped}_{ELM}} = \exp(-(\Delta_{Wall} + \Delta_{ELM})/\lambda_{ELM}) \tag{43}$$

. Splitting the energy deposited onto the divertor target plates into tiles #3 and #7 (covered by IR, near strike line) and #1 and #8 (based on TC, remote of strike line) corresponding expressions for the divertor target plates are found to be

$$f_{\#1+\#8} = \frac{E_{ELM}^{\#1+\#8}}{E_{ELM}^{ped}} = \exp(-(\Delta_{IR} + \Delta_{ELM})/\lambda_{ELM}) - f_{Wall} \tag{44}$$

and

$$f_{\#3+\#7} = \frac{E_{ELM}^{IR}}{E_{ELM}^{ped}} = 1 - f_{\#1+\#8} - f_{Wall} \tag{45}$$

In [60] inter-change driven amplitude scaling for $v_\perp$ with convective ion losses on the ELM size (E_{ELM}^{ped} $/E_{ped}$) [61, 62] is proposed giving $\chi = 0.5$. The results from reciprocating probe at JET show roughly a linear dependence between the ELM related amount of particles arriving at the probe and the ELM radial propagation (see also Figure 6 in [2]) and suggest a value for $\chi \approx 1.0$. Therefore, in Figure 19 the experimental data are compared to estimates for $\chi = 0.5$ and $\chi = 1.0$.

The size of Δ_{ELM} will be at maximum in the range of the ELM affected radial width in the pedestal region due to edge ergodisation of the separatrix during the ELM event [63] and at minimum zero. The exact separatrix location is possibly furthermore affected by a movement of the entire plasma column due to ELM related current losses [64, 65, 66]. The whole situation can be of course even more complex due to the generic non-toroidal symetric structure of ELMs (and resulting heat load) [24, 42].

Generally good agreement between the simple formalism giving $f_{\#3+\#7}$ and the experimental results is found (data are identical to the data presented in figure 14). The calculated values for $f_{\#3+\#7}$ is shown for three different values of Δ_{ELM}, namely $\Delta_{ELM} = 0$, $\Delta_{ELM} = \Delta_{ped}/2 = 1.5cm$ and $\Delta_{ELM} = \Delta_{ped} = 3.0$ cm. Best agreement is found for $\Delta_{ELM} = \Delta_{ped}/2 = 1.5cm$, but also for $\Delta_{ELM} = 3.0cm$ the agreement is reasonable. Therefore, without a better knowledge on the exact separatrix structure during ELMs (which requires excellent knowledge of the instability process itself and is beyond current diagnostics resolution) allowing for a better quantification for Δ_{ELM} further conclusion based on the presented measurements appear to be impossible. Nevertheless, it may is worth notifying, that also in the work on the ELM wall load to JET and ITER in [60] the so called mid-pedestal value $\Delta_{ELM} = \Delta_{ped}/2 = 1.5cm$ is regarded to describe the experimental data best.

For $f_{\#1+\#8}$ and $\chi = 0.5, \Delta_{ELM} = \Delta_{ped}/2 = 1.5cm$ the simple formalism shows less good agreement to the experimental data. Here, systemaically lower experimental values are observed than calculated. A possible explanation is given here. The same fraction of ELM to Inter-ELM energy deposition is assumed for the remote tiles (#1 and #8) as for the tiles close to the strike line (#3 and #7). From ASDEX Upgrade it is reported that the dominant fraction of the wall loading is due to ELMs [67] being roughly 1.5 times larger than the energy deposited on the first wall in the inter-ELM periods, where for the power deposition to the strike lines as commonly observed in tokomaks the dominant fraction comes between ELMs (see also Figure 18 (a)). Therefore it appears

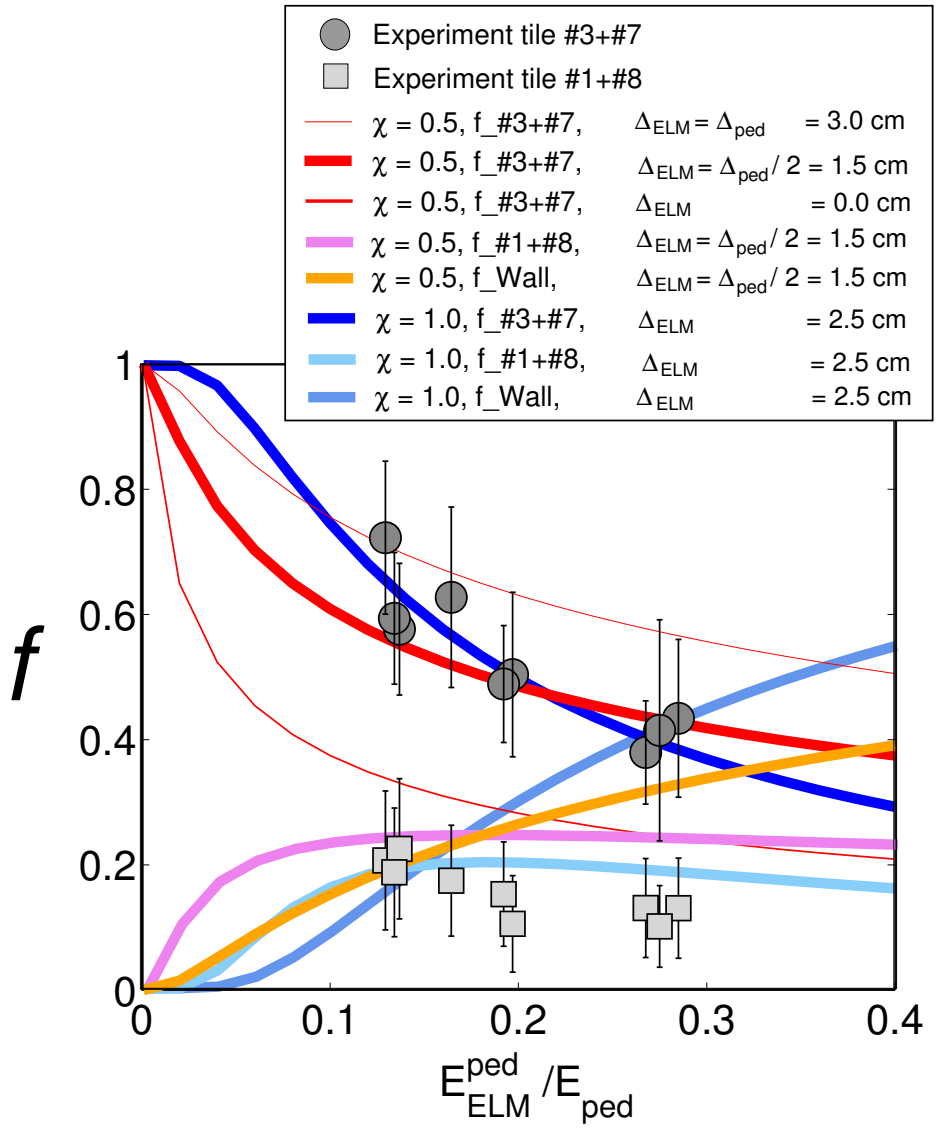

Figure 19. Comparison of the experimental data to simple estimates as described in the text. Circles show the ELM energies regarding tile#3 and #7 (near strike line) and squares tile #1 and #8 (remote of strike line).

to be plausible that a higher fraction of the energy onto the remote divertor target tiles (#1 and #8) is due to ELMs than measured for the target tiles close to the strike line (#3 and #7).

However, it is of great importance to note that even for a value for $\chi = 1.0$, which is more in line with the ELM velocity dependence on ELM size as measured by reciprocating probes at the first wall in JET[59] and *not* based on the interchange-driven amplitude scaling, and applying $\Delta_{ELM} = 2.5cm$ fair agreement is found within the errorbars. Extending this excercise also to the target tiles #1 and #8 for $\chi = 1.0$ and $\Delta_{ELM} = 2.5cm$ even slightly better agreement compared to the interchange-driven model is found but appears, following the discussion above, still not to be conclusive.

Finally, the expected heat load to the wall is presented. Comparing the two sets of curves corresponding to either $\chi = 0.5$ or $\chi = 1.0$ an important aspect should be noted. For the commonly observed ELM sizes at JET (and other tokamaks) with ELM loss energies between 0.1 and 0.3 of the pedestal energy the differences between the corresponding f for the divertor target plates or the wall calculated by assuming $\chi = 0.5$ or $\chi = 1.0$ stay small. It is therefore experimentally hard to separate which model assumption is better. Larger differences should be existent for very small ELM sizes of a few percent, but then experimental errorbars become much larger.

The presented results are consistent to an ELM propagation across the SOL where larger ELMs have larger radial propagation velocities. However, due to the large errorbars of the presented data, particlarly the uncertainty of the exact separatrix location during the ELM and the few data points avalaible for ELM resolved measurements in the JET Gas Box divertor, no conclusion are given about the scaling of $v_\perp/c_s$. For an extended discussion on ELM radial propagation and underlying transport processes see also e.g. [68, 69, 70, 71, 72].

Further effects due to radiation have been completely ignored in the presented analysis since this effect, following the discussion above, is assumed to be small for JET. In ASDEX Upgrade 50% of the ELM pedestal loss energy is found on the divertor targets [73], with a fraction in the range of 10% to 40% radiated during the ELM, so much larger than it is assumed to be the case in the analysed discharges presented here. The radiated fraction of the ELM loss energy in ASDEX Upgrade clearly decreases with increasing normalised ELM size. The largest amount of energy to be radiated during an ELM in ASDEX Upgrade does not exceed 10kJ[74]. IR thermography of the ASDEX Upgrade first wall [67] has provided direct evidence that $\approx$ 15% of the ELM energy in similar discharges is deposited on wall structures mainly near the outer equatorial midplane.

The divertor density and temperature values in JET and ASDEX Upgrade are comparable [75, 76]. The divertor volume differs by a factor of about two whereas the absolute ELM energy loss in JET is 10-20 times larger than in ASDEX Upgrade. It is therefore conjectured that in JET a larger fraction of the ELM pedestal energy loss is transported towards the main chamber than in ASDEX Upgrade and that in return the radiated fraction in JET is lower than in ASDEX Upgrade. However, direct evidence for the main chamber power load is necessary to evaluate the ELM energy load there in detail. Therefore a new IR wide angle camera to observe the first wall components has been recently brought into operation in JET[77, 78]. First results from JET confirm that ELMs deposit a non negligible amount of energy onto the outer equatorial midplane limiters leading to high temperature excursions of the plasma facing surface of these limiters. [79]

This is an important issue for ITER since if the ELM pedestal loss energy is to the same extent transported to the main chamber walls it could cause significant erosion/melting, particularly if, as is currently foreseen, Beryllium components are used. For ELMs in ITER an upper limit of tolerable ELM size in terms of energy loss and

resulting thermal ablation of divertor target material (not including e.g. micro-cracking) regarding the divertor life time is given by about E^{IR}_{ELM} /E^{ped}_{ELM} =5% (with an absolute size of about 6MJ[41]) to E^{IR}_{ELM} /E^{ped}_{ELM} =10% (with an absolute size of about 11MJ[2]). Only for such *small* ELMs in ITER, the fraction of expected ELM energy wall load is then expected to be comparable small.

5. Acknowledgements

The authors like to thank many of the JET-EFDA colleagues involved in the C1-C4 campaigns. In particular the authors would like to mention the discussions and collaborations with A.V.Chankin, J.P.Coad, K.H.Finken, J.C.Fuchs, E.Gauthier, S.Jachmich, A.Kallenbach, H.R.Koslowski, M.Laux, G.F.Matthews, R.Neu, V.Philipps, J.Rapp, V.Riccardo, W.Suttrop and J.Vince.

6. References

[1] ITER Physics Expert Group, Nuclear Fusion **39**, 2137 (1999).
[2] T. Eich *et al.*, J.Nucl.Mater. **337-339**, 669 (2005).
[3] F. Schueller, Plas.Phys.Contr.Fusion **37**, A135 (1995).
[4] H. Zohm, Plas.Phys.Contr.Fusion **38**, 105 (1996).
[5] F. Wagner *et al.*, Phys. Rev. Lett. **49**, 1408 (1982).
[6] A. Chankin *et al.*, Plas.Phys.Contr.Fusion **36**, 403 (1994).
[7] S. Clement *et al.*, J.Nucl.Mater. **266-269**, 285 (1999).
[8] V. Rohde *et al.*, J.Nucl.Mater. **290-293**, 317 (2001).
[9] V. Rohde *et al.*, J.Nucl.Mater. **313-316**, 337 (2003).
[10] D. Storek and K. Gentle, Nuclear Fusion **41**, 1 (2001).
[11] P. Andrew *et al.*, J.Nucl.Mater. **313-316**, 135 (2003).
[12] P. Andrew *et al.*, J.Nucl.Mater. **337-339**, 99 (2005).
[13] E. Gauthier *et al.*, J.Nucl.Mater. **337-339**, 960 (2005).
[14] R. Reichle *et al.*, J.Nucl.Mater. **313-316**, 711 (2003).
[15] E. Delchambre *et al.*, J.Nucl.Mater. **337-339**, 1069 (2005).
[16] A. Herrmann *et al.*, Physica Scripta **111**, 98 (2004).
[17] T. Eich *et al.*, J.Nucl.Mater. **313-316**, 919 (2003).
[18] A. Herrmann *et al.*, Plas.Phys.Contr.Fusion **37**, 17 (1995).
[19] V. Riccardo *et al.*, Plas.Phys.Contr.Fusion **43**, 881 (2001).
[20] J. P. Coad *et al.*, J.Nucl.Mater. **313-316**, 419 (2003).
[21] Y. Corre *et al.*, 'Surface layer properties estimation for JET DOC-L discharges' in Contributions to 30th Conference on Controlled Fusion and Plasma Physics, St.Petersburg, Russia (2003).
[22] A. Herrmann *et al.*, 'Limitations for Divertor Heat Flux Calculations of Fast Events in Tokamaks' in Contribution to 27th Conference to Plasma Physics and Controlled Fusion, Madeira, Portugal (2001).
[23] R. A. Pitts *et al.*, J.Nucl.Mater. **337-339**, 146 (2005).
[24] T. Eich *et al.*, Phys.Rev.Letter **91**, 195003 (2003).
[25] T. Eich *et al.*, Plas.Phys.Contr.Fusion **47**, 815 (2005).
[26] E. Delchambre *et al.*, J.Nucl.Mater., accepted for publication (2007).
[27] A. Kallenbach *et al.*, Plas.Phys.Contr.Fusion **46**, 431 (2004).
[28] H. Zohm *et al.*, Nuclear Fusion **35**, 543 (1995).
[29] A. Loarte *et al.*, Physics of Plasmas **11**, 2668 (2004).

[30] A. Leonard *et al.*, Physics of Plasmas **10**, 1765 (2003).
[31] N. Oyama *et al.*, Nuclear Fusion **44**, 582 (2004).
[32] J. Likonen *et al.*, Fusion Eng. Design **66-68**, 219 (2003).
[33] J. Likonen *et al.*, J.Nucl.Mater. **337-339**, 60 (2005).
[34] A. Kirschner *et al.*, Plas.Phys.Contr.Fusion **45**, 309 (2003).
[35] R. A. Pitts *et al.*, Plas.Phys.Contr.Fusion **47**, B303 (2005).
[36] G. F. Matthews *et al.*, J.Nucl.Mater. **290-293**, 668 (2001).
[37] D. L. Rudakov *et al.*, Plas.Phys.Contr.Fusion **44**, 717 (2002).
[38] G. F. Matthews *et al.*, Nuclear Fusion **39**, 19 (1999).
[39] J. Rapp *et al.*, Plas.Phys.Contr.Fusion **44**, 639 (2002).
[40] A. Loarte *et al.*, Nuclear Fusion **38**, 331 (1998).
[41] A. Loarte *et al.*, Plas.Phys.Contr.Fusion **45**, 1549 (2003).
[42] A. Kirk *et al.*, Phys.Rev.Letter **92**, 245002 (2004).
[43] B. Kurzan *et al.*, Phys.Rev.Letter **95**, 145001 (2005).
[44] R. Sartori *et al.*, 'Scaling Study of ELMy H-mode global and pedestal confinement at high triangularity in JET', presented at IAEA Fusion Energy Conference, Vilamoura, Portugal (2004).
[45] J. W. Connor, Plas.Phys.Contr.Fusion **40**, 191 (1998).
[46] A. Loarte *et al.*, J.Nucl.Mater. **313-316**, 962 (2003).
[47] G. Saibene *et al.*, Plas.Phys.Contr.Fusion **44**, 1769 (2002).
[48] A. Loarte *et al.*, Plas.Phys.Contr.Fusion **44**, 1815 (2002).
[49] W. Fundamenski *et al.*, Nuclear Fusion **45**, 950 (2005).
[50] A. Chankin, J.Nucl.Mater. **241-243**, 199 (1997).
[51] T. Eich *et al.*, J.Nucl.Mater.,accepted for publication (2007).
[52] J. Rapp *et al.*, J.Nucl.Mater. **337-339**, 826 (2005).
[53] P. Monier-Garbet *et al.*, Nucl.Fusion **45**, 1404 (2005).
[54] J. Rapp *et al.*, Nuclear Fusion **44**, 312 (2004).
[55] A. Loarte *et al.*, IAEA Fusion Energy Conference, Sorrento, Italy (2000).
[56] R. A. Pitts *et al.*, Nuclear Fusion **46**, 82 (2006).
[57] W. Fundamenski and R. Pitts, Plas.Phys.Contr.Fusion **48**, 109 (2006).
[58] W. Fundamenski *et al.*, Plas.Phys.Contr.Fusion **46**, 233 (2004).
[59] C. Silva *et al.*, J.Nucl.Mater. **337-339**, 722 (2005).
[60] W. Fundamenski *et al.*, J.Nucl.Mater., accepted for publication .
[61] O. Garcia *et al.*, Plas.Phys.Contr.Fusion **48**, L1 (2006).
[62] O. Garcia *et al.*, Physics of Plasmas **13**, 082309 (2006).
[63] H. Koslowski *et al.*, Nuclear Fusion **45**, 201 (2005).
[64] J. Lingertat *et al.*, J.Nucl.Mater. **241-243**, 402 (1997).
[65] E. Solano *et al.*, J.Nucl.Mater. **337-339**, 747 (2005).
[66] D. Testa *et al.*, Plas.Phys.Contr.Fusion **47**, 733 (2005).
[67] A. Herrmann *et al.*, Plas.Phys.Contr.Fusion **46**, 971 (2004).
[68] S. Krasheninnikov, Physics Letters A **283**, 368 (2001).
[69] A. Kirk *et al.*, Phys.Rev.Letter **96**, 185001 (2006).
[70] O. Grulke *et al.*, Physics of Plasmas **13**, 012306 (2006).
[71] J. Terry *et al.*, J.Nucl.Mater. **337-339**, 322 (2005).
[72] M. Endler *et al.*, Plasma Physics and Controlled Fusion **47**, 219 (2005).
[73] A. Herrmann *et al.*, J.Nucl.Mater. **313-316**, 759 (2003).
[74] J. C. Fuchs *et al.*, Journal of Nuclear Materials **337-339**, 756 (2005).
[75] A. Kallenbach *et al.*, Plas.Phys.Contr.Fusion **41**, B177 (1999).
[76] A. Chankin *et al.*, Plas.Phys.Contr.Fusion **48**, 839 (2006).
[77] P. Andrew *et al.*, J.Nucl.Mater., accepted (2006).
[78] E. Gauthier *et al.*, Contribution to SOFT conference-2006 (2006).

[79] E. Gauthier *et al.*, J.Nucl.Mater., accepted (2006).